Geothermal Energy

RESEARCH Open Access

# Petrophysical properties of the Muschelkalk from the Soultz-sous-Forêts geothermal site (France), an important lithostratigraphic unit for geothermal exploitation in the Upper Rhine Graben

Michael J. Heap[1*], Alexandra R. L. Kushnir[1], H. Albert Gilg[2], Marie E. S. Violay[3], Pauline Harlé[4] and Patrick Baud[1]

*Correspondence: heap@unistra.fr
[1] Géophysique Expérimentale, Institut de Physique de Globe de Strasbourg (UMR 7516 CNRS, Université de Strasbourg/EOST), 5 Rue René Descartes, 67084 Strasbourg Cedex, France
Full list of author information is available at the end of the article

## Abstract

The Muschelkalk, composed of Triassic limestones, marls, dolomites, and evaporites, forms part of the Permo-Triassic cover of sedimentary rocks that directly overlies the fractured granitic reservoir used for geothermal energy exploitation in the Upper Rhine Graben. Petrophysical data for this lithostratigraphic unit are sparse, but are of value for reservoir prospection, stimulation, and optimisation strategies at existing and prospective geothermal sites throughout the Upper Rhine Graben. To this end, we present here a systematic microstructural, mineralogical, and petrophysical characterisation of the Muschelkalk core (from the Middle to Lower Muschelkalk; from a depth of ~ 930 to ~ 1001 m) from exploration borehole EPS-1 at Soultz-sous-Forêts (France). First, we assessed the microstructure and mineral content of samples from six depths that we consider represent the variability of the available core. The majority of the core is composed of fine-grained, interbedded dolomites and marls; however, anhydrite and a dolomitic sandstone bank were found in the Upper and Lower Muschelkalk core, respectively. A larger suite of samples (from fifteen depths, including the six depths chosen for microstructural and mineral content analysis) were then characterised in terms of their petrophysical properties. The matrix porosity of the measured Muschelkalk samples is low, from ~ 0.01 to ~ 0.1, and their matrix permeability is below the resolution of our permeameter ($\ll 10^{-18}$ m$^2$). P-wave velocity, thermal conductivity, thermal diffusivity, specific heat capacity per unit volume, Young's modulus, and uniaxial compressive strength range from 2.60 to 5.37 km/s, 2.42 to 5.72 W/mK, 1.19 to 2.46 mm$^2$/s, 1.63 to 2.46 MJ/m$^3$ K, 9.4 to 39.5 GPa, and 55.1 to 257.6 MPa, respectively. Therefore, and despite the narrow range of porosity, the petrophysical properties of the Muschelkalk are highly variable. We compare these new data with those recently acquired for the Buntsandstein unit (the Permo-Triassic unit immediately below the Muschelkalk) and thus provide an overview of the petrophysical properties of the two sedimentary units that directly overly the fractured granitic reservoir.

**Keywords:** Muschelkalk, Porosity, P-wave velocity, Thermal properties, Uniaxial compressive strength, Microstructure, Geothermal, Upper Rhine Graben

## Introduction

Geothermal energy projects within the Upper Rhine Graben, a 350-km-long and 50-km-wide Cenozoic rift valley, exploit anonymously high geothermal gradients (> 80 °C/km) that are attributed to crustal thinning and efficient large-scale hydrothermal convection (e.g., Ledésert et al. 1996; Pribnow and Schellschmidt 2000; Buchmann and Connolly 2007; Guillou-Frottier et al. 2013; Baillieux et al. 2013; Magnenet et al. 2014; Vallier et al. 2018, 2019). Indeed, more than fifteen geothermal wells have been drilled in the Upper Rhine Graben since the 1980s (Vidal and Genter 2018). The geology of the region consists of a fractured granitic basement (e.g., Ledésert et al. 1993; Genter and Traineau 1996; Genter et al. 1997; Hooijkaas et al. 2006; Sausse et al. 2006; Dezayes et al. 2010; Genter et al. 2010; Villeneuve et al. 2018; Glaas et al. 2018) overlain by a sequence of Permian and Triassic sedimentary rocks (Buntsandstein, Muschelkalk, and Keuper; e.g., Haffen et al. 2013; Vidal et al. 2015; Griffiths et al. 2016; Aichholzer et al. 2016, 2019; Heap et al. 2017; Kushnir et al. 2018a, b; Heap et al. 2018, 2019; Duringer et al. 2019; Harlé et al. 2019), Jurassic sedimentary rocks, and Tertiary to Quaternary graben fill (e.g., Berger et al. 2005; Hinsken et al. 2007, 2011; Aichholzer et al. 2016; Duringer et al. 2019) (Fig. 1c).

The Buntsandstein unit, a ~ 400-m-thick sequence of sandstones (Fig. 1c) (e.g., Aichholzer et al. 2016; Heap et al. 2017), and the Muschelkalk unit, a ~ 100-m-thick sequence of Triassic limestones, marls, dolomites, and evaporites (Fig. 1c) (e.g., Aichholzer et al. 2016; Duringer et al. 2019), are considered to form the top of the regional convection zone (e.g., Vidal et al. 2015; Baujard et al. 2017). Both units are known to be laterally extensive in the Upper Rhine Graben (e.g., Sittler 1969; Brun and Wenzel 1991). The permeability required to support large-scale hydrothermal convection in the Buntsandstein

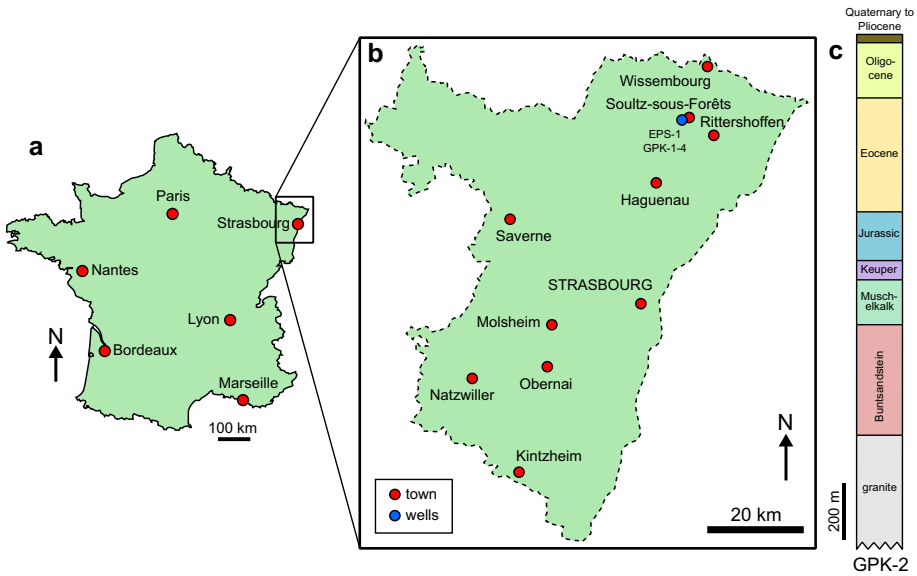


**Fig. 1** **a** Map of France showing the location of Strasbourg. **b** Map of the Bas-Rhin department showing the location of several towns and cities, including Soultz-sous-Forêts and Rittershoffen, and EPS-1 exploration well and the GPK-1-4 wells at Soultz-sous-Forêts (blue circle). **c** Stratigraphic column showing the stratigraphy at the Soultz-sous-Forêts geothermal site (for GPK-2; Aichholzer et al. 2016). The reservoir granite was encountered down to the final drilling depth of 5080 m (not shown here)

and Muschelkalk units is provided by faults and fractures (e.g., Vidal et al. 2015; Kushnir et al. 2018a). In the Muschelkalk unit, the focus of the present study, there is ample evidence for permeable fractured zones (e.g., Reyer et al. 2012; Meier et al. 2015; Vidal et al. 2015; Aichholzer et al. 2016). For example, Reyer et al. (2012) and Meier et al. (2015) analysed fault zones within the Muschelkalk unit with displacements ranging from a few centimetres to a few tens of metres in northwest and southeast Germany, respectively. Many of the faults described in these studies appear related to the regional stress field associated with the Upper Rhine Graben, in which intra-graben faults strike dominantly NNW (with subsidiary NNE and NW sets) and faults on the border of the graben strike between NW and NE (Peters and van Balen 2007; see also Schumacher 2002; Cardozo and Behrmann 2006; Meixner et al. 2016). The faults studied by Reyer et al. (2012) and Meier et al. (2015) are also associated with damage zones containing fractures preferentially orientated parallel to the fault strike. Within France, the correlation of stratigraphic logs from Soultz-sous-Forêts and Rittershoffen (locations given in Fig. 1b) suggests the presence of faults within the Muschelkalk (Aichholzer et al. 2016). The two permeable zones in the Muschelkalk identified in the GPK-2 and GPK-3 wells at Soultz-sous-Forêts have apparent thicknesses between 5 and 20 m; the orientation of these faults, however, is challenging to interpret in the absence of imaging logging (Vidal et al. 2015). The Buntsandstein and Muschelkalk units are not only important for regional hydrothermal convection, but recent and forthcoming geothermal projects have also targeted the interface between the fractured granitic basement and these overlying Permo-Triassic sedimentary rocks. The Muschelkalk unit, for example, is also used as a hot water aquifer at the geothermal plant at Riehen in Switzerland (in the Upper Rhine Graben; e.g., Link et al. 2015). As a result, the petrophysical properties of the rocks forming the Buntsandstein and Muschelkalk units form essential input parameters in thermo-hydro-mechanical modelling designed to better understand large-scale fluid circulation, heat flow calculations, and temperature estimations and can be used to guide reservoir stimulation strategies and assessments of borehole stability.

Recent experimental studies have explored the microstructural and petrophysical properties of the Permo-Triassic Buntsandstein lithostratigraphic unit (Fig. 1c). Heap et al. (2017), for example, measured the porosity, permeability, and P-wave velocity of sandstones from exploration borehole EPS-1 at the Soultz-sous-Forêts geothermal site (France) (Fig. 1a, b). These authors found that the porosity, P-wave velocity, and permeability of these sandstones vary from ~ 0.03 to 0.2, ~ 2.5 to 4.5 km/s, and ~ $10^{-18}$ to $10^{-13}$ $m^2$, respectively. The low porosity, high P-wave velocity, and the low permeability of the sandstones comprising the top (*Grès à Voltzia* and *Couches Intermédiaires* formations) and bottom (*Grès d'Annweiler* and *Grès anté-Annweiler* formations) were considered by these authors to be a result of pore-filling alteration (Heap et al. 2017). The uniaxial compressive strength and Young's modulus of Buntsandstein sandstones from EPS-1 were found to range from ~ 50 MPa and ~ 10 GPa, respectively, for a porosity of ~ 0.25 and up to ~ 250 MPa and ~ 40 GPa, respectively, for a porosity of ~ 0.04 (Heap et al. 2019). These authors also showed that the uniaxial compressive strength and Young's modulus are reduced when the sandstones are saturated with water (Heap et al. 2019). Further, Heap et al. (2018) found that the uniaxial compressive strength and Young's modulus of Buntsandstein sandstones from EPS-1 saturated with the in situ brine (from production

well GPK-2 at Soultz-sous-Forêts; Fig. 1b) do not differ from those saturated with water. However, there are no corresponding data for the overlying Muschelkalk lithostratigraphic unit (Fig. 1c). We present here, therefore, a systematic microstructural, mineralogical, and petrophysical characterisation of the Muschelkalk core (from the Middle to Lower Muschelkalk; from a depth of ~ 930 to ~ 1001 m) from exploration borehole EPS-1 at Soultz-sous-Forêts (Fig. 1a, b). EPS-1 provides full core (diameter = 78 mm) of the part of the Muschelkalk lithostratigraphic unit, the lowermost part of the Middle Muschelkalk and the entire Lower Muschelkalk (from ~ 930 to ~ 1001 m). Due to the availability of core material at EPS-1, Soultz-sous-Forêts represents an ideal case study for investigating the microstructural and petrophysical properties of the Muschelkalk. As mentioned above, these data can be used to assist reservoir prospection, stimulation, and optimisation strategies at geothermal sites throughout the Upper Rhine Graben, and particularly those that use, or plan to use, the Muschelkalk unit as a reservoir/aquifer (e.g., the geothermal project at Riehen; Link et al. 2015).

## Materials and methods

The Muschelkalk lithostratigraphic unit is the middle part of the Triassic sedimentary sequence encountered in the Upper Rhine Graben. The Muschelkalk is characterised by marine-to-lagoonal environment deposits (limestones and dolomites) that are rich in marine fauna (e.g., Ménillet 2015; Aichholzer et al. 2016, 2019; Duringer et al. 2019). The Muschelkalk is divided, from the top to the base, into three members corresponding to different depositional environments (Ménillet 2015; Duringer et al. 2019; Aichholzer et al. 2019). (1) The Upper Muschelkalk, which is characterised by massive limestone at its base and alternating marls and limestones at its top. (2) The Middle Muschelkalk, which is mainly composed of silty and carbonatic clayey layers with occasional evaporitic deposits (gypsum and anhydrite). (3) The Lower Muschelkalk, which is characterised by shelly and sandy marls and marly clays. The Muschelkalk core at EPS-1 contains the following formations (see Duringer et al. (2019) and Aichholzer et al. (2019) for more detailed descriptions). (1) *Marnes Bariolées* (Middle Muschelkalk), which comprises red and grey silty clays and greenish dolomitic marls. Dolomitic banks are also present and are increasingly abundant at the top of the formation. This formation also contains evaporites (anhydrite and gypsum) and probable hydraulic breccias. (2) *Couches à Orbicularis* and *Schaumkalk* complex (Lower Muschelkalk), which comprises alternating silty to clayey compact dolomitic banks and siltstone or clay joints. (3) *Calcaires Ondulés* (or *Wellenkalk*) (Lower Muschelkalk) which comprises thin layers (about 1 cm thick) of dolomitic limestone with frequent siltstone or marly joints. This formation owes its name to the wavy appearance of the rock as a result of asymmetric ripple marks and flute casts. (4) *Wellenmergel* and *Couches à Térébratules* (Lower Muschelkalk), which mostly comprises fine sandstones and variably dolomitic sandy mudstones. Some dolomitic sandstone and grainy dolostone banks are encountered in the lowermost part of the formation. Crinoid and terebratula (a genus of brachiopods) fossils can sometimes be found, giving the formation its name. (5) *Couches à Myacites* (Lower Muschelkalk), which comprises marls and carbonates with rare sandstone banks and dolomitic lenses. (6) *Grès Coquillier* (Lower Muschelkalk), the lowermost formation in the Muschelkalk,

which comprises calcareous or dolomitic sandstone rich in shell debris and bioturbations interbedded with clayey marl beds.

We sampled the Muschelkalk lithostratigraphic unit at fifteen regularly spaced depth intervals between the top (at ~ 930 m) and the bottom (at ~ 1001 m) of the cored interval from the EPS-1 exploration well at the Soultz-sous-Forêts geothermal site (Fig. 2). Four samples were selected from the *Marnes Bariolées* (Middle Muschelkalk) (from core boxes 6, 19, 22 and 29). The remaining eleven samples were taken from the Lower Muschelkalk: two from the *Couches à Orbicularis* and *Schaumkalk* complex (from boxes 29, 32, and 36), one from the *Calcaires Ondulés* (or *Wellenkalk*) (from box 45), four from the *Wellenmergel* and *Couches à Térébratules* (from boxes 52, 53, 59, and 61), two from the *Couches à Myacites* (from boxes 64 and 66), and two from the *Grès Coquillier* (from boxes 70 and 73) (Fig. 2). We also sampled Buntsandstein sandstone core from three depth intervals at the interface between the Muschelkalk and the Buntsandstein units (from boxes 76, 81, and 82), unsampled in our previous petrophysical studies (Heap et al. 2017, 2018; Kushnir et al. 2018a; Heap et al. 2019) (Fig. 2).

We first chose six samples from our fifteen depth intervals to perform detailed microstructural and mineralogical analysis. These six samples, from boxes 6 and 22 from the Middle Muschelkalk and boxes 32, 45, 59, and 61 from the Lower Muschelkalk (see

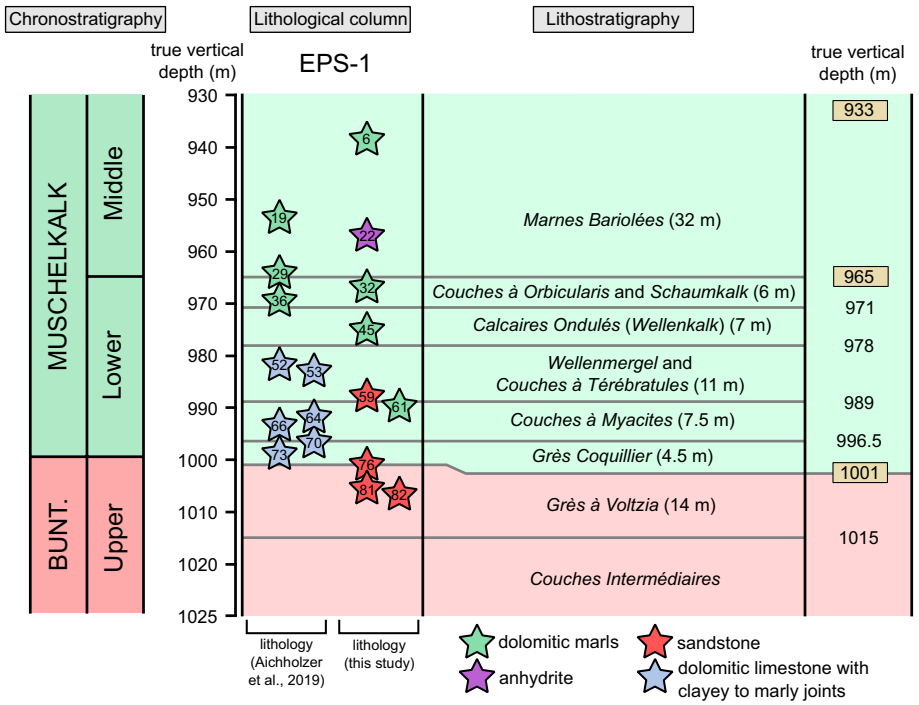


**Fig. 2** Chronostratigraphic and lithological columns showing the names, thicknesses, and depths (true vertical depth) of the formations within the Muschelkalk and the top of the Buntsandstein for exploration well EPS-1 (Soultz-sous-Forêts). The approximate depths of the sampled core, fifteen depths in total, are indicated by the stars. The number within the star corresponds to the box number from which the sample was taken, and the colour of the star reflects the lithology (see key at the bottom of the figure). The lithology was either determined using the mineral contents determined using X-ray powder diffraction (this study, see Table 1) or was taken from Aichholzer et al. 2019)

Fig. 2 for depths), were selected as they were considered to best represent the variability of the available core. We also performed microstructural and mineralogical analysis on the three samples of Buntsandstein sandstone taken from the interface between the Muschelkalk and the Buntsandstein units (see Fig. 2 for depths). Double-polished thin sections for each of the nine depth intervals were prepared to investigate their microstructures using a scanning electron microscope (SEM) (Tescan Vega 2 XMU) in backscattered mode. The mineral content of the nine samples was quantified using X-ray powder diffraction (XRPD). Powdered offcuts of the core material were ground for 8 min with 10 ml of isopropyl alcohol in a McCrone Micronising Mill using $ZrO_2$ cylinder elements. The XRPD analyses were performed on powder mounts using a Bruker D8 Advance Eco X-ray diffractometer (CuKα, 40 kV, 25 mA, 2°–75° 2$\Theta$, 0.01° step size, 20 mm irradiated length, 2.5° primary and secondary sollers and a LynxEye XE-T detector). The phases in the whole rock powders were then quantified using the Rietveld program BGMN (Bergmann et al. 1998) and the Profex graphical user interface (Döbelin and Kleeberg 2015). To identify clay minerals, we also separated < 2 μm fractions by gravitational settling and prepared oriented mounts that were X-rayed in an air-dried state, an ethylene-glycolated state, and following exposure to 550 °C.

One to four cylindrical samples, 20 mm in diameter and precision ground to a nominal length of 35–40 mm, were extracted from each of the eighteen sampled depths. The samples were cored so that their axes were parallel to the EPS-1 borehole (i.e., perpendicular to bedding). These samples were then washed to remove any soluble grinding fluid and oven-dried at 40 °C in a vacuum oven for at least 48 h. Photographs of representative 20-mm-diameter samples from each of the eighteen sampled depths are provided in Fig. 3.

The connected porosity of each sample was determined using the bulk volume calculated using the sample dimensions and the connected (skeletal) volume measured by a helium pycnometer (Micromeritics AccuPyc II 1340). P-wave velocity was measured under a uniaxial stress of ~ 1 MPa along the axis of each sample using piezoelectric sensors excited at a frequency of 700 kHz. The length of the sample and the time of the first arrival of the signal through the sample were used to calculate the P-wave velocity. The permeability of the samples was assessed using a benchtop gas (nitrogen) permeameter (schematic provided in Farquharson et al. 2016; Heap and Kennedy 2016) under a confining pressure of 1 MPa. However, we found that the permeability of all the prepared Muschelkalk samples was below the resolution of our permeameter ($\ll 10^{-18}$ m$^2$). Thermal diffusivity and thermal conductivity were measured (and specific heat capacity per unit volume calculated) for each depth interval using two 20-mm-diameter cylindrical samples either side of a Kapton sensor (3.189 mm in radius) and a Hot Disk TPS 500 Thermal Constants Analyser (more details are provided in Gustavsson et al. 1994; Harlé et al. 2019). A series of four consecutive measurements was performed on the different sample surfaces. Each measurement was performed at least 5 min apart to ensure that the sample had cooled back to the ambient temperature. To check whether the sample had cooled back to ambient temperature, the sensor measured the temperature of the sample for 40 s prior to each measurement. If the sample temperature was not constant during

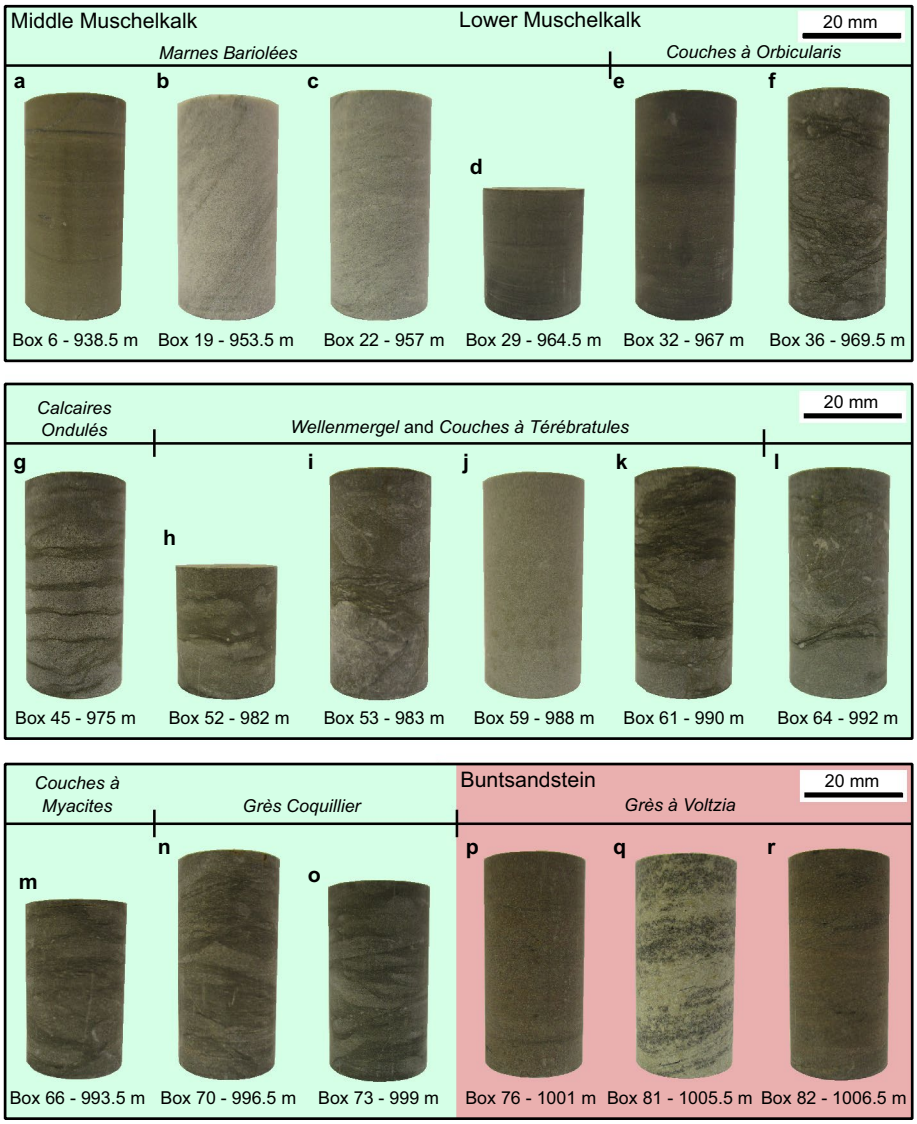


**Fig. 3** Representative photographs of the Muschelkalk (**a**–**o**) and Buntsandstein (**p**–**r**) samples (20 mm in diameter) from exploration well EPS-1 (Soultz-sous-Forêts) used for this study. The box number and measured depth are given next to each photograph

this 40 s period, the data were not considered and the measurement was repeated. The reported values are averages of these four measurements. Finally, the prepared cylindrical samples were deformed uniaxially at a strain rate of $1.0 \times 10^{-5}$ $s^{-1}$ until macroscopic failure. During deformation, axial displacement and axial load were measured using two linear variable differential transducers (LVDT) and a load cell, respectively. These measurements were converted to axial strain (using the average displacement from the two transducers) and axial stress using the sample dimensions. The static Young's modulus of each sample was determined from the elastic portion

of the stress–strain curves. We adopt the convention that compressive stresses and strains are positive.

## Results

### Microstructural and mineralogical analyses

The mineral contents for the six samples chosen to represent the variability the Muschelkalk, from boxes 6 and 22 from the Middle Muschelkalk and boxes 32, 45, 59, and 61 from the Lower Muschelkalk, and the three samples taken from the very top of the Buntsandstein (boxes 76, 81, and 82), are given in Table 1. Figures 4 and 5 show backscattered SEM images of the nine samples.

The sample from box 6 (*Marnes Bariolées*, Middle Muschelkalk; 938.5 m; Fig. 3a) is a very fine-grained (~ 10 μm; Figs. 4a, 5a) dolomite (86 wt%) with minor quartz (7 wt%), calcite (3 wt%), muscovite/illite (3 wt%), and K-feldspar (1 wt%) (Table 1). The dolomite grains are angular and much of the inter-particle porosity is filled with clay (Fig. 5a). Sample 6 also contains calcite-filled fractures (Fig. 4a).

The sample from box 22 (*Marnes Bariolées*, Middle Muschelkalk; 957 m; Fig. 3c) is mostly composed of anhydrite (88 wt%), with some dolomite (11 wt%) and minor quartz (1 wt%) (Table 1). Individual grains are typically ~ 25–50 μm in diameter, and the pores have a diameter between ~ 10 and 20 μm (Figs. 4a, 5a). Sample 22 contains sample-scale slump structures and deformed laminations (Fig. 3c), evidence of soft-sediment deformation. We consider sample 19 (Fig. 3b) to have a very similar microstructure and mineral content to sample 22.

The sample from box 32 (*Couches à Orbicularis* and *Schaumkalk* complex, Lower Muschelkalk; 967 m; Fig. 3e) is a very fine-grained (~ 10–40 μm; Figs. 4c, 5c) marly dolomite (74 wt% dolomite and 18 wt% muscovite/illite) with minor quartz (4 wt%), K-feldspar (3 wt%), and pyrite (1 wt%) (Table 1). Similar to the sample from box 6, the dolomite grains are angular and much of the inter-particle porosity is filled with clay (Fig. 5c). We consider sample 29 (Fig. 3d) to have a very similar microstructure and mineral content to sample 32.

The sample from box 45 (*Calcaires Ondulés* or *Wellenkalk*, Lower Muschelkalk; 975 m; Fig. 3g) is a fine-grained (~ 100–150 μm; Figs. 4d, 5d) marly dolomite (85 wt% dolomite and 10 wt% muscovite/illite) with minor quartz (4 wt%) and K-feldspar (1 wt%) (Table 1). On the sample scale, sample 45 contains regularly spaced, and wavy, marly lenses (Fig. 3g).

The sample from box 59 (*Wellenmergel* and *Couches à Térébratules*, Lower Muschelkalk; 988 m; Fig. 3j) is a homogeneous, fine-grained (~ 50–100 μm; Figs. 4e, 5e) dolomitic sandstone (45 wt% quartz and 26 wt% dolomite) with muscovite/illite (16 wt%), K-feldspar (10 wt%), and minor siderite (3 wt%) (Table 1). The pores in sample 59 (~ 50 μm in diameter) are filled with clay (Figs. 4e, 5e).

The sample from box 61 (*Couches à Myacites*, Lower Muschelkalk; 990 m; Fig. 3k) is a very fine-grained (~ 10–50 μm; Figs. 4f, 5f) marly dolomite (68 wt% dolomite and 20 wt% muscovite/illite) with minor quartz (8 wt%), K-feldspar (3 wt%), and siderite (1 wt%) (Table 1). Similar to the samples from box 6 and 32, the dolomite grains are angular and much of the inter-particle porosity is filled with clay (Fig. 5f). We consider sample 61 (Fig. 3k) to have a very similar microstructure and mineral content to a large portion

**Table 1 X-ray powder diffraction (XRPD) analysis showing quantitative bulk mineralogical composition for the six Muschelkalk samples chosen to represent the variability of the Muschelkalk at exploration well EPS-1 (Soultz-sous-Forêts), and three samples from the Buntsandstein at the Muschelkalk–Buntsandstein interface**

| Lithostratigraphic unit | Formation | True vertical depth (m) | Box number | Anhydrite | Dolomite | Siderite | Calcite | Quartz | K-feldspar | Muscovite/illite | Pyrite |
|---|---|---|---|---|---|---|---|---|---|---|---|
| Middle Muschelkalk | Marnes Bariolées | 938.5 | 6 | – | 86 | – | 3 | 7 | 1 | 3 | – |
| Middle Muschelkalk | Marnes Bariolées | 957 | 22 | 88 | 11 | – | – | 1 | – | – | – |
| Lower Muschelkalk | Couches à Orbicularis and Schaumkalk complex | 967 | 32 | – | 74 | – | – | 4 | – | 18 | 1 |
| Lower Muschelkalk | Calcaires Ondulés | 975 | 45 | – | 85 | – | – | 5 | 1 | 10 | – |
| Lower Muschelkalk | Wellenmergel and Couches à Térébratules | 988 | 59 | – | 26 | 3 | – | 45 | 10 | 16 | – |
| Lower Muschelkalk | Wellenmergel and Couches à Térébratules | 990 | 61 | – | 68 | 1 | – | 8 | 3 | 20 | – |
| Buntsandstein | Grès à Voltzia | 1001 | 76 | – | 1 | 9 | – | 58 | 3 | 29 | – |
| Buntsandstein | Grès à Voltzia | 1005.5 | 81 | – | 4 | 2 | – | 66 | 10 | 18 | – |
| Buntsandstein | Grès à Voltzia | 1006.5 | 82 | – | 11 | 4 | – | 46 | 4 | 35 | – |

Values in wt%

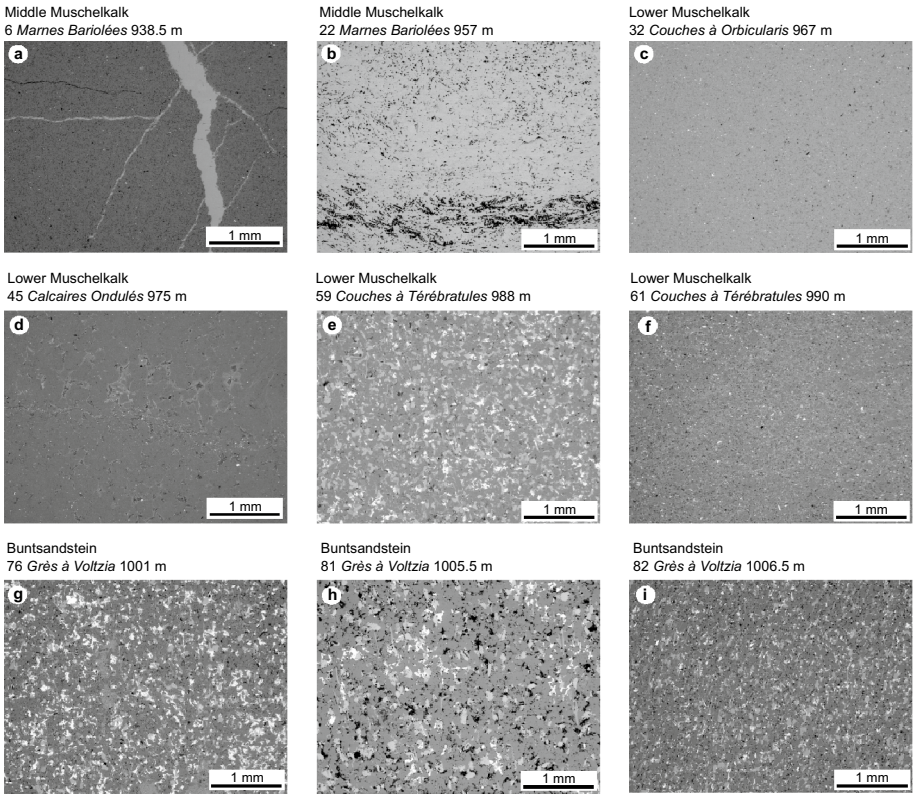


**Fig. 4** Backscattered scanning electron microscope images showing the microstructure of the six Muschelkalk samples chosen to represent the variability of the Muschelkalk at exploration well EPS-1 (Soultz-sous-Forêts) (**a**–**f**), and three samples from the Buntsandstein at the Muschelkalk–Buntsandstein interface (**g**–**i**). The lithological unit, box number, and measured depth are given next to each image

of the EPS-1 core (i.e., the majority of the core comprises marly dolomite), including samples from boxes 36 (Fig. 3f), 52 (Fig. 3h), 53 (Fig. 3i), 64 (Fig. 3l), 66 (Fig. 3m), 70 (Fig. 3n), and 73 (Fig. 3o).

The sample from box 76 (*Grès à Voltzia*, Buntsandstein; 1001 m; Fig. 3p) is a fine-grained (~ 25–100 µm; Figs. 4g, 5g) marly sandstone (58 wt% quartz and 29 wt% muscovite/illite) with minor siderite (9 wt%), K-feldspar (3 wt%), and dolomite (1 wt%). The pores in sample 76 (~ 50 µm in diameter) are filled with siderite and clay (Figs. 4g, 5g).

The sample from box 81 (*Grès à Voltzia*, Buntsandstein; 1005.5 m; Fig. 3q) is a fine-grained (~ 50–100 µm; Figs. 4h, 5h) marly sandstone (66 wt% quartz and 18 wt% muscovite/illite) with K-feldspar (10 wt%) and minor dolomite (4 wt%) and siderite (2 wt%) (Table 1). Some pores in sample 81 (~ 50 µm in diameter) are filled with siderite and clay, whilst others only contain a coating of clay or no filling (Figs. 4h, 5h).

The sample from box 82 (*Grès à Voltzia*, Buntsandstein; 1006.5 m; Fig. 3r) is a fine-grained (~ 50–100 µm; Figs. 4i, 5i) marly sandstone (46 wt% quartz and 35 wt% muscovite/illite) with dolomite (11 wt%) and minor K-feldspar (4 wt%) and siderite (4 wt%) (Table 1). Much of the inter-particle porosity is filled with clay and siderite (Figs. 4i, 5i).

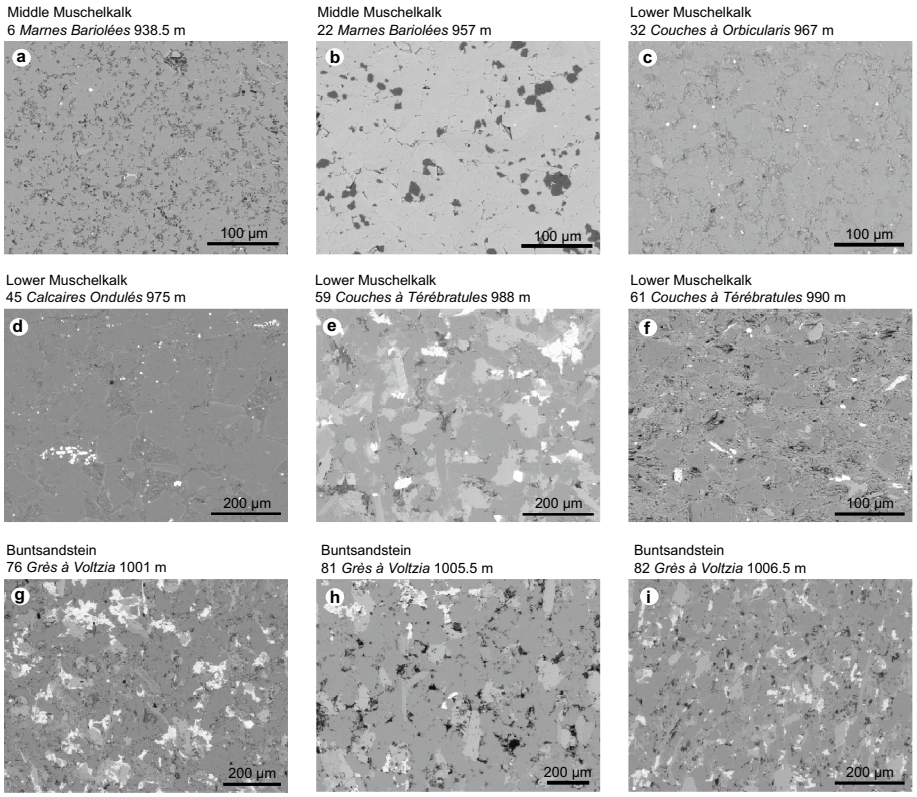


**Fig. 5** Zoomed backscattered scanning electron microscope images showing the microstructure (the pore and grain size in particular) of the six Muschelkalk samples chosen to represent the variability of the Muschelkalk at exploration well EPS-1 (Soultz-sous-Forêts) (**a**–**f**), and three samples from the Buntsandstein at the Muschelkalk–Buntsandstein interface (**g**–**i**). The lithological unit, box number, and measured depth are given next to each image

The grains in sample 82 are elongate and appear to be preferentially orientated sub-parallel to the core axis (i.e., sub-parallel to the drilling orientation) (Figs. 4i, 5i).

In summary, a large portion of the Muschelkalk core from the EPS-1 exploration borehole at Soultz-sous-Forêts comprises fine-grained (~ 100–150 µm) to very fine-grained (~ 10–50 µm) marly dolomites that are characterised by very small pore sizes (~ 5–25 µm) (Figs. 4, 5). Apart from sample 6 (*Marnes Bariolées*, Middle Muschelkalk; Fig. 4a), we did not observe microcracks in any of the samples studied (Figs. 4, 5).

### Petrophysical analyses

The connected matrix porosity of the Muschelkalk samples measured ranges between ~ 0.01 and ~ 0.1 (Table 2). The majority of the samples have porosities less than 0.05 (Table 2). The highest porosity, ~ 0.1, is found in the sample from box 6 (*Marnes Bariolées*, Middle Muschelkalk) (Table 2). P-wave velocity is plotted as a function of porosity in Fig. 6 (data available in Table 2). The P-wave velocity of the Muschelkalk samples measured ranges between 2.60 and 5.37 km/s (Fig. 6). Excluding the sample from box 6 (*Marnes Bariolées*, Middle Muschelkalk), which has a high P-wave velocity despite its high porosity, there is a general trend of decreasing P-wave velocity as porosity increases (Fig. 6). The thermal conductivity, thermal diffusivity, and specific

**Table 2 Summary of the laboratory data (connected porosity, P-wave velocity, Young's modulus, and uniaxial compressive strength) collected for the fifteen depths sampled in the Muschelkalk at exploration well EPS-1 (Soultz-sous-Forêts), and three depths sampled in the Buntsandstein at the Muschelkalk–Buntsandstein interface**

| Lithostratigraphic unit | Formation | True vertical depth (m) | Box number | Connected porosity (–) | Dry P-wave velocity (km/s) | Young's modulus (GPa) | Uniaxial compressive strength (MPa) |
|---|---|---|---|---|---|---|---|
| Middle Muschelkalk | Marnes Bariolées | 938.5 | 6 | 0.10 | 4.96 | 34.6 | 207.9 |
| Middle Muschelkalk | Marnes Bariolées | 938.5 | 6 | 0.10 | 4.89 | – | – |
| Middle Muschelkalk | Marnes Bariolées | 953.5 | 19 | 0.00 | 5.29 | 33.6 | 106.8 |
| Middle Muschelkalk | Marnes Bariolées | 953.5 | 19 | 0.00 | 5.34 | 35.0 | 117.0 |
| Middle Muschelkalk | Marnes Bariolées | 957 | 22 | 0.01 | 3.99 | 34.7 | 135.4 |
| Middle Muschelkalk | Marnes Bariolées | 957 | 22 | 0.01 | 4.34 | 33.7 | 129.9 |
| Middle Muschelkalk | Marnes Bariolées | 964.5 | 29 | 0.02 | 5.36 | – | – |
| Lower Muschelkalk | Couches à Orbicularis and Schaumkalk complex | 967 | 32 | 0.06 | 3.72 | 20.9 | 169.8 |
| Lower Muschelkalk | Couches à Orbicularis and Schaumkalk complex | 967 | 32 | 0.06 | 3.70 | 20.7 | 169.8 |
| Lower Muschelkalk | Couches à Orbicularis and Schaumkalk complex | 969.5 | 36 | 0.03 | 3.95 | 22.2 | 119.6 |
| Lower Muschelkalk | Couches à Orbicularis and Schaumkalk complex | 969.5 | 36 | 0.03 | 4.80 | – | – |
| Lower Muschelkalk | Calcaires Ondulés | 975 | 45 | 0.04 | 3.56 | – | – |
| Lower Muschelkalk | Calcaires Ondulés | 975 | 45 | 0.04 | 3.84 | 23.6 | 119.4 |
| Lower Muschelkalk | Calcaires Ondulés | 975 | 45 | 0.04 | 2.60 | 27.4 | 134.7 |
| Lower Muschelkalk | Calcaires Ondulés | 975 | 45 | 0.04 | 3.37 | 21.8 | 118.2 |
| Lower Muschelkalk | Wellenmergel and Couches à Térébratules | 982 | 52 | 0.03 | 4.04 | – | – |

**Table 2 (continued)**

| Lithostratigraphic unit | Formation | True vertical depth (m) | Box number | Connected porosity (–) | Dry P-wave velocity (km/s) | Young's modulus (GPa) | Uniaxial compressive strength (MPa) |
|---|---|---|---|---|---|---|---|
| Lower Muschelkalk | Wellenmergel and Couches à Térébratules | 982 | 52 | 0.05 | 3.80 | – | – |
| Lower Muschelkalk | Wellenmergel and Couches à Térébratules | 983 | 53 | 0.02 | 4.80 | 35.2 | 187.6 |
| Lower Muschelkalk | Wellenmergel and Couches à Térébratules | 983 | 53 | 0.02 | 5.03 | 39.5 | 200.8 |
| Lower Muschelkalk | Wellenmergel and Couches à Térébratules | 988 | 59 | 0.04 | 4.43 | 34.5 | 252.6 |
| Lower Muschelkalk | Wellenmergel and Couches à Térébratules | 988 | 59 | 0.04 | 4.46 | 34.6 | 257.6 |
| Lower Muschelkalk | Wellenmergel and Couches à Térébratules | 990 | 61 | 0.03 | 3.67 | 17.6 | 67.5 |
| Lower Muschelkalk | Wellenmergel and Couches à Térébratules | 990 | 61 | 0.05 | 3.40 | – | – |
| Lower Muschelkalk | Couches à Myacites | 992 | 64 | 0.02 | 4.95 | 35.2 | 177.8 |
| Lower Muschelkalk | Couches à Myacites | 992 | 64 | 0.03 | 4.56 | 27.6 | 128.3 |
| Lower Muschelkalk | Couches à Myacites | 993.5 | 66 | 0.04 | 3.55 | – | – |
| Lower Muschelkalk | Couches à Myacites | 993.5 | 66 | 0.05 | 4.03 | – | – |
| Lower Muschelkalk | Grès Coquillier | 996.5 | 70 | 0.05 | 3.24 | 13.8 | 56.9 |
| Lower Muschelkalk | Grès Coquillier | 996.5 | 70 | 0.05 | 3.26 | – | – |
| Lower Muschelkalk | Grès Coquillier | 996.5 | 70 | 0.05 | 3.49 | 9.4 | 55.1 |
| Lower Muschelkalk | Grès Coquillier | 996.5 | 70 | 0.04 | 4.02 | – | – |

**Table 2 (continued)**

| Lithostratigraphic unit | Formation | True vertical depth (m) | Box number | Connected porosity (–) | Dry P-wave velocity (km/s) | Young's modulus (GPa) | Uniaxial compressive strength (MPa) |
|---|---|---|---|---|---|---|---|
| Lower Muschelkalk | Grès Coquillier | 999 | 73 | 0.04 | 3.57 | 19.7 | 130.7 |
| Lower Muschelkalk | Grès Coquillier | 999 | 73 | 0.04 | 3.74 | 20.6 | 139.1 |
| Lower Muschelkalk | Grès Coquillier | 999 | 73 | 0.04 | 3.62 | 19.3 | 120.7 |
| Buntsandstein | Grès à Voltzia | 1001 | 76 | 0.03 | 4.32 | 32.2 | 241.6 |
| Buntsandstein | Grès à Voltzia | 1001 | 76 | 0.03 | 4.24 | 31.9 | 241.3 |
| Buntsandstein | Grès à Voltzia | 1005.5 | 81 | 0.10 | 3.37 | 21.3 | 134.5 |
| Buntsandstein | Grès à Voltzia | 1005.5 | 81 | 0.10 | 3.39 | 22.5 | 150.1 |
| Buntsandstein | Grès à Voltzia | 1006.5 | 82 | 0.04 | 3.07 | 20.5 | 175.0 |
| Buntsandstein | Grès à Voltzia | 1006.5 | 82 | 0.04 | 3.02 | 19.3 | 152.8 |

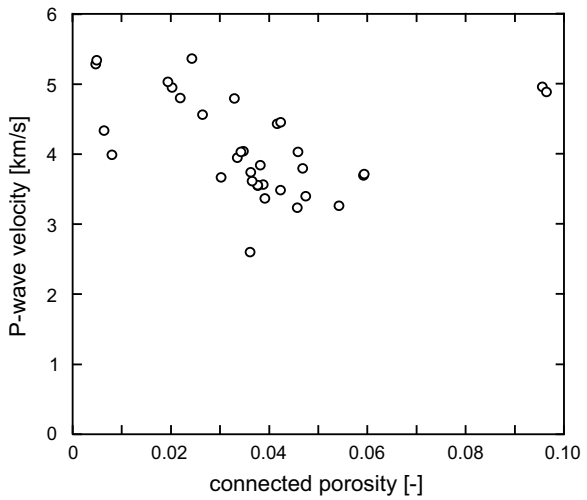


**Fig. 6** Dry P-wave velocity (measured at ambient pressure and temperature) as a function of connected porosity for Muschelkalk samples from exploration well EPS-1 (Soultz-sous-Forêts)

heat capacity of the Muschelkalk samples are plotted as a function of porosity in Fig. 7 (data available in Table 3). The thermal conductivity, thermal diffusivity, and specific heat capacity range, respectively, from 2.42 to 5.72 W/mK, 1.19 to 2.46 $mm^2/s$, 1.63 to 2.46 $MJ/m^3K$ (Fig. 7). All three properties appear to decrease as a function of increasing porosity, although the trend is less clear for specific heat capacity (Fig. 7). Representative uniaxial stress–strain curves for the Muschelkalk samples are provided in Fig. 8a. These uniaxial stress–strain curves are typical of those for rocks deforming in compression (e.g., Eberhardt et al. 1999). Stress is initially a non-linearly increasing function of

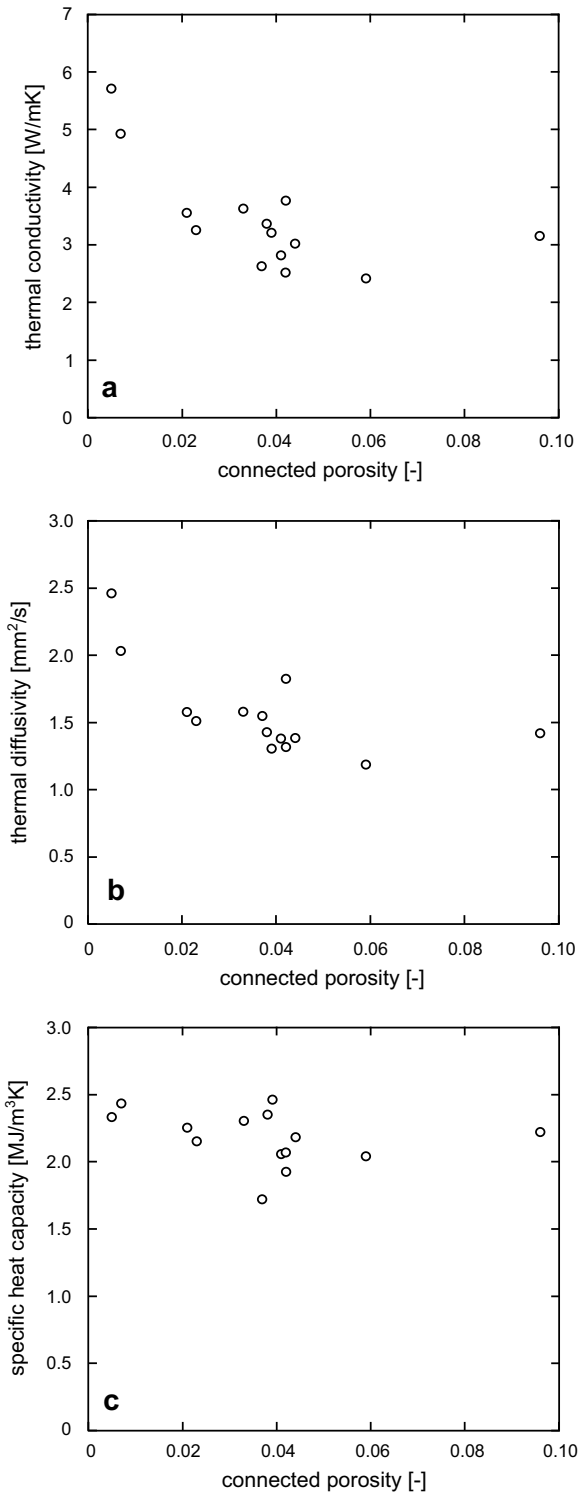


**Fig. 7** **a** Dry thermal conductivity **b** dry thermal diffusivity, and **c** dry specific heat capacity per unit volume as a function of connected porosity for Muschelkalk samples from exploration well EPS-1 (Soultz-sous-Forêts)

**Table 3 Summary of the laboratory thermal property data (thermal conductivity, thermal diffusivity, and specific heat capacity per unit volume) for samples from the Muschelkalk and Buntsandstein sampled from exploration well EPS-1 (Soultz-sous-Forêts)**

| Lithostratigraphic unit | Formation | Measured depth (m) | Box number | Average connected porosity (-) | Thermal conductivity (W/mK) | Thermal diffusivity ($mm^2/s$) | Specific heat capacity per unit volume ($MJ/m^3K$) |
|---|---|---|---|---|---|---|---|
| Middle Muschelkalk | Marnes Bariolées | 938.5 | 6 | 0.10 | 3.159 | 1.423 | 2.221 |
| Middle Muschelkalk | Marnes Bariolées | 953.5 | 19 | 0.01 | 5.720 | 2.462 | 2.334 |
| Middle Muschelkalk | Marnes Bariolées | 957 | 22 | 0.01 | 4.932 | 2.032 | 2.433 |
| Lower Muschelkalk | Couches à Orbicularis and Schaumkalk complex | 967 | 32 | 0.06 | 2.421 | 1.186 | 2.041 |
| Lower Muschelkalk | Couches à Orbicularis and Schaumkalk complex | 369.5 | 36 | 0.03 | 3.637 | 1.581 | 2.304 |
| Lower Muschelkalk | Calcaires Ondulés | 975 | 45 | 0.04 | 3.368 | 1.431 | 2.355 |
| Lower Muschelkalk | Wellenmergel and Couches à Térébratules | 982 | 52 | 0.04 | 2.825 | 1.379 | 2.058 |
| Lower Muschelkalk | Wellenmergel and Couches à Térébratules | 983 | 53 | 0.02 | 3.557 | 1.578 | 2.255 |
| Lower Muschelkalk | Wellenmergel and Couches à Térébratules | 988 | 59 | 0.04 | 3.771 | 1.825 | 2.069 |
| Lower Muschelkalk | Wellenmergel and Couches à Térébratules | 990 | 61 | 0.04 | 3.214 | 1.305 | 2.464 |
| Lower Muschelkalk | Couches à Myacites | 992 | 64 | 0.02 | 3.259 | 1.511 | 2.156 |
| Lower Muschelkalk | Couches à Myacites | 993.5 | 66 | 0.04 | 2.522 | 1.317 | 1.927 |
| Lower Muschelkalk | Grès Coquillier | 996.5 | 70 | 0.04 | 3.020 | 1.386 | 2.183 |
| Lower Muschelkalk | Grès Coquillier | 999 | 73 | 0.04 | 2.629 | 1.550 | 1.720 |
| Buntsandstein | Grès à Voltzia | 1001 | 76 | 0.03 | 3.636 | 2.006 | 1.818 |
| Buntsandstein | Grès à Voltzia | 1005.5 | 81 | 0.10 | 3.199 | 1.970 | 1.628 |
| Buntsandstein | Grès à Voltzia | 1006.5 | 82 | 0.04 | 2.614 | 1.510 | 1.733 |
| Buntsandstein | Grès à Voltzia | 1008 | 84 | 0.09 | 3.450 | 2.122 | 1.625 |
| Buntsandstein | Couches Intermédiaires | 1022 | 100 | 0.06 | 3.611 | 2.094 | 1.727 |
| Buntsandstein | Karlstal | 1069 | 157 | 0.11 | 3.813 | 2.592 | 1.475 |
| Buntsandstein | Karlstal | 1107 | 198 | 0.09 | 3.830 | 2.327 | 1.654 |
| Buntsandstein | Karlstal | 1151 | 248 | 0.14 | 3.432 | 2.166 | 1.619 |

**Table 3 (continued)**

| Lithostratigraphic unit | Formation | Measured depth (m) | Box number | Average connected porosity (-) | Thermal conductivity (W/mK) | Thermal diffusivity ($mm^2/s$) | Specific heat capacity per unit volume ($MJ/m^3K$) |
|---|---|---|---|---|---|---|---|
| Buntsandstein | Rehberg | 1197 | 299 | 0.12 | 3.320 | 2.069 | 1.619 |
| Buntsandstein | Rehberg | 1239 | 347 | 0.18 | 2.993 | 1.805 | 1.660 |
| Buntsandstein | Trifels | 1290 | 402 | 0.13 | 3.264 | 1.865 | 1.750 |
| Buntsandstein | Trifels | 1336 | 453 | 0.18 | 2.597 | 1.786 | 1.455 |
| Buntsandstein | Grès d'Annweiler | 1376 | 497 | 0.04 | 3.831 | 2.223 | 1.728 |
| Buntsandstein | Grès d'Annweiler | 1386 | 508 | 0.08 | 3.073 | 1.702 | 1.806 |
| Buntsandstein | Grès anté-Annweiler | 1414 | 540 | 0.07 | 2.684 | 1.557 | 1.726 |

strain (often attributed to the closure of pre-existing microcracks and flaws), followed by a quasi-linear elastic portion, a region where stress is a non-linearly decreasing function of strain (often attributed to the formation and growth of new microcracks), and, finally, a stress drop associated with the macroscopic failure of the sample (Fig. 8a). The uniaxial compressive strength the Muschelkalk samples, plotted as a function of porosity in Fig. 8b (data available in Table 2), ranges from 55.1 to 257.6 MPa. We observe no trend between uniaxial compressive strength and porosity (Fig. 8b). Young's modulus is plotted as a function of porosity in Fig. 8c (data available in Table 2). The Young's modulus of the Muschelkalk samples measured ranges between 9.4 and 39.5 GPa (Fig. 8c). Excluding the sample from box 6 (*Marnes Bariolées*, Middle Muschelkalk), which has a high Young's modulus despite its high porosity, there is a general trend of increasing Young's modulus as porosity decreases (Fig. 8c).

## Discussion

### Petrophysical properties

Our data show that the P-wave velocity (Fig. 6), thermal conductivity (Fig. 7a), thermal diffusivity (Fig. 7b), specific heat capacity (Fig. 7c), and Young's modulus (Fig. 8c) of the measured Muschelkalk samples decrease as a function of increasing porosity. Because rock-forming minerals have a higher P-wave velocity than air, the P-wave velocity of dry rocks is commonly seen to decrease as porosity increases (Fig. 6) (e.g., Han et al. 1986, Eberhart-Phillips et al. 1989; Chang et al. 2006). Similarly, the thermal conductivity, thermal diffusivity, and specific heat capacity of air are much lower than those for rock-forming minerals, explaining the decrease in these properties as a function of increasing porosity (Fig. 7) (e.g., Brigaud and Vasseur 1989; Bagdassarov and Dingwell 1994; Clauser and Huenges 1995; Popov et al. 2003; Pimienta et al. 2014; Esteban et al. 2015). Although P-wave velocity (e.g., Han et al. 1986; Eberhart-Phillips et al. 1989) and thermal conductivity (e.g., Brigaud and Vasseur 1989), for example, are also known to vary as a function of increasing clay content, we see no systematic variation in our data as a function of clay content (i.e., muscovite/illite; Tables 1 and 2). We also note that the P-wave

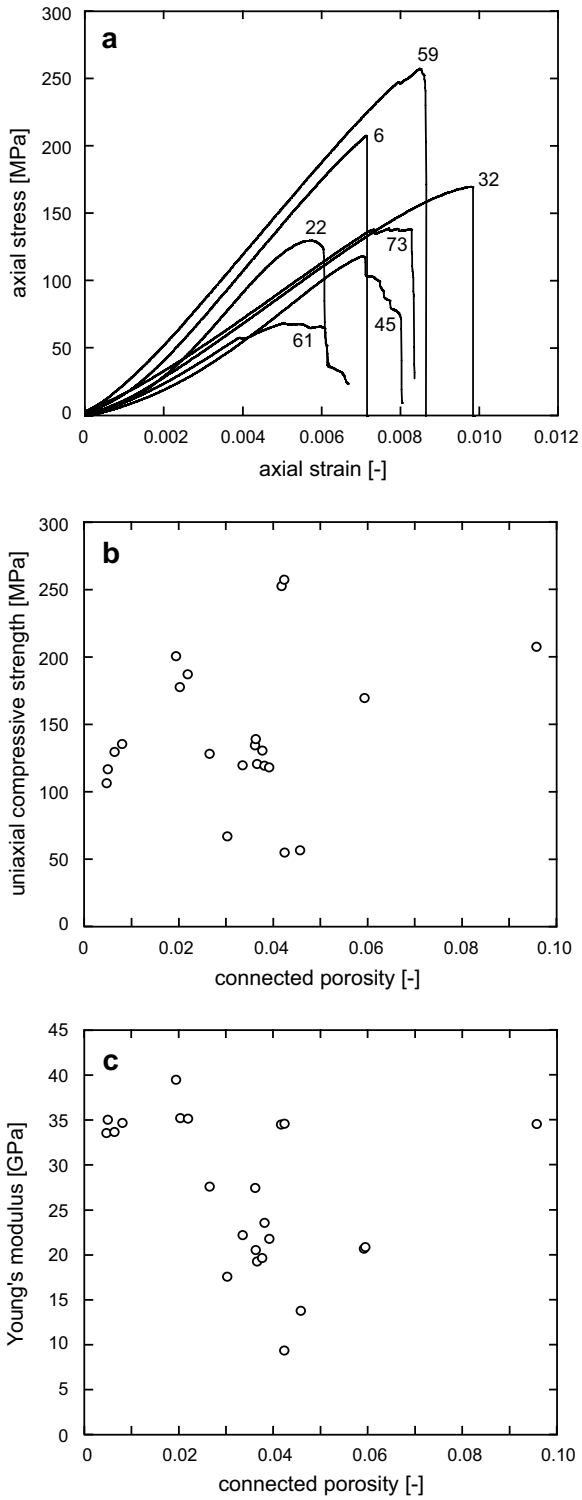


**Fig. 8** **a** Representative dry stress–strain curves (box number indicated next to each curve), **b** dry uniaxial compressive strength as a function of connected porosity, and **c** dry Young's modulus as a function of connected porosity for Muschelkalk samples from exploration well EPS-1 (Soultz-sous-Forêts)

velocities of the Muschelkalk samples are much lower (by about 1 km/s) than carbonates of the same porosity (Regnet et al. 2015, 2019) and is likely the result of the textural (Fig. 3), microstructural (Figs. 4, 5), and compositional (Table 1) complexity of the Muschelkalk samples studied. Because rock-forming minerals also have a higher stiffness than air, the Young's modulus of rock typically decreases as porosity increases (e.g., Chang et al. 2006; Griffiths et al. 2017), as seen in our experimental data (Fig. 8c). However, we observe no trend between uniaxial compressive strength and porosity (Fig. 8b). The uniaxial compressive strength of rock typically decreases as a function of increasing porosity (e.g., Sammis and Ashby 1986; Chang et al. 2006; Heap et al. 2014; Baud et al. 2014). We attribute the observed scatter in uniaxial compressive strength (Fig. 8b) as a result of textural (Fig. 3), microstructural (Figs. 4, 5), and compositional (Table 1) variations between our Muschelkalk samples. For example, the strongest sample, from box 59 (*Wellenmergel* and *Couches à Térébratules*, Lower Muschelkalk; Fig. 3j), is the only sandstone we sampled from the Muschelkalk core at EPS-1. Further, the samples of anhydrite (boxes 19 and 22; *Marnes Bariolées*, Middle Muschelkalk; Figs. 3d, 3e) have the lowest porosities of the samples measured (< 0.01; Table 2) but have relatively low uniaxial compressive strengths (between 107 and 135 MPa; Fig. 8b; Table 2). Low-porosity anhydrite has been shown previously to have a relatively low uniaxial compressive strength (~ 80 to ~ 127 MPa; Bell 1994 and ~ 52 to ~ 144 MPa; Trippetta et al. 2013) and undergo the transition from brittle to ductile behaviour at relatively low effective pressures (De Paola et al. 2009). We also note that our values of uniaxial compressive strength and Young's modulus of the Muschelkalk unit compare well with similar measurements provided by Reyer et al. (2012). These authors measured one sample from each of the Upper (from Hessenbühl, Germany) and Lower (from Emmenhausen, Germany) Muschelkalk units and found uniaxial compressive strengths of 90 and 150 MPa, respectively, and Young's moduli of 37 and 50 GPa, respectively (Reyer et al. 2012).

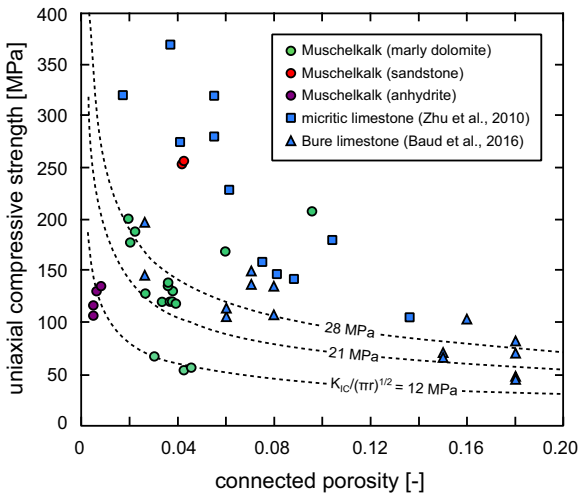


**Fig. 9** Uniaxial compressive strength as a function of connected porosity for the studied Muschelkalk samples from exploration well EPS-1 (Soultz-sous-Forêts) and for published data for limestones from Zhu et al. (2010) and Baud et al. (2016). Three modelled curves are provided using the analytical solution of the Sammis and Ashby (1986) pore-emanating crack model provided by Zhu et al. (2010) (Eq. (1); see text for details)

To provide more insight as to the mechanical behaviour of the Muschelkalk samples studied, we compare the strength of our Muschelkalk samples with data for carbonate rocks compiled by Zhu et al. (2010) and Baud et al. (2016) in Fig. 9. For a given porosity, the strength of the Muschelkalk samples is comparable with that of highly cemented allochemical limestones from Bure (France; Baud et al. 2016), but is significantly lower than the micritic limestones presented in Zhu et al. (2010) (Fig. 9). Because experimental studies have shown that dolomite is mechanically stronger than calcite (e.g., Delle Piane et al. 2009; Kushnir et al. 2015), the lower strength of the Muschelkalk samples highlights the importance of clay in dictating their mechanical behaviour. We also provide modelled curves of uniaxial compressive strength ($\sigma_u$) as a function of porosity ($\phi$) using analytical solution for the pore-emanating crack model of Sammis and Ashby (1986) provided by Zhu et al. (2010) (Fig. 9):

$$\sigma_u = \frac{1.325}{\phi^{0.414}} \frac{K_{\mathrm{IC}}}{\sqrt{\pi r}}, \tag{1}$$

where $K_{IC}$ is the fracture toughness and $r$ is the pore radius. If we focus on the marly dolomites, and exclude the two outliers characterised by high strengths and high porosities, we can bracket our data between curves for which $\frac{K_{\mathrm{IC}}}{\sqrt{\pi r}}$ is equal to 12 and 28 MPa (Fig. 9). We find a range of pore diameters of ~ 10 to ~ 50 μm (the range of pore sizes observed in our microstructural analysis; Figs. 4, 5) using a constant value of $K_{\mathrm{IC}}$ of 0.11 MPa $m^{1/2}$, a value much closer to the $K_{\mathrm{IC}}$ of clay (the $K_{\mathrm{IC}}$ of Mancos shale was measured to be between 0.12 and 0.44 MPa $m^{1/2}$; Chandler et al. 2016) than to that of dolomite (2.47 MPa $m^{1/2}$; Austin and Kennedy 2005). This micromechanical modelling therefore reinforces the first-order importance of clay in governing the mechanical properties of the Muschelkalk samples studied.

#### Comparison with the Buntsandstein unit

The new petrophysical data for the Muschelkalk unit (and the three Buntsandstein samples from the Buntsandstein–Muschelkalk interface, within the *Grès à Voltzia* formation) collected for this study (Table 2) can now be compared with similar data collected for the Buntsandstein unit (data from Heap et al. 2017, 2018, 2019). Figure 10 presents the P-wave velocity, uniaxial compressive strength, and Young's modulus as a function of porosity for both the Muschelkalk and Buntsandstein units. We highlight that the Buntsandstein typically has a much higher matrix porosity, and a much wider range of porosity, than the Muschelkalk (Fig. 10). However, despite this larger range of porosity, and the aforementioned first-order control of porosity on rock physical properties, the petrophysical properties of the rocks forming the Muschelkalk vary considerably (Fig. 10). In other words, the range of P-wave velocity, uniaxial compressive strength, and Young's modulus is larger for the Muschelkalk than for the Buntsandstein, despite the narrow porosity distribution of the Muschelkalk and the wide porosity distribution of the Buntsandstein (Fig. 10). We consider this a consequence of the large textural (Fig. 3), microstructural (Figs. 4, 5), and compositional (Table 1) variations within the Muschelkalk unit. By contrast, the Buntsandstein unit comprises solely sandstones, most of which are feldspathic sandstones with varying quantities of clay (muscovite/illite–smectite) (e.g., Heap et al. 2017). An important difference between the Muschelkalk and Buntsandstein

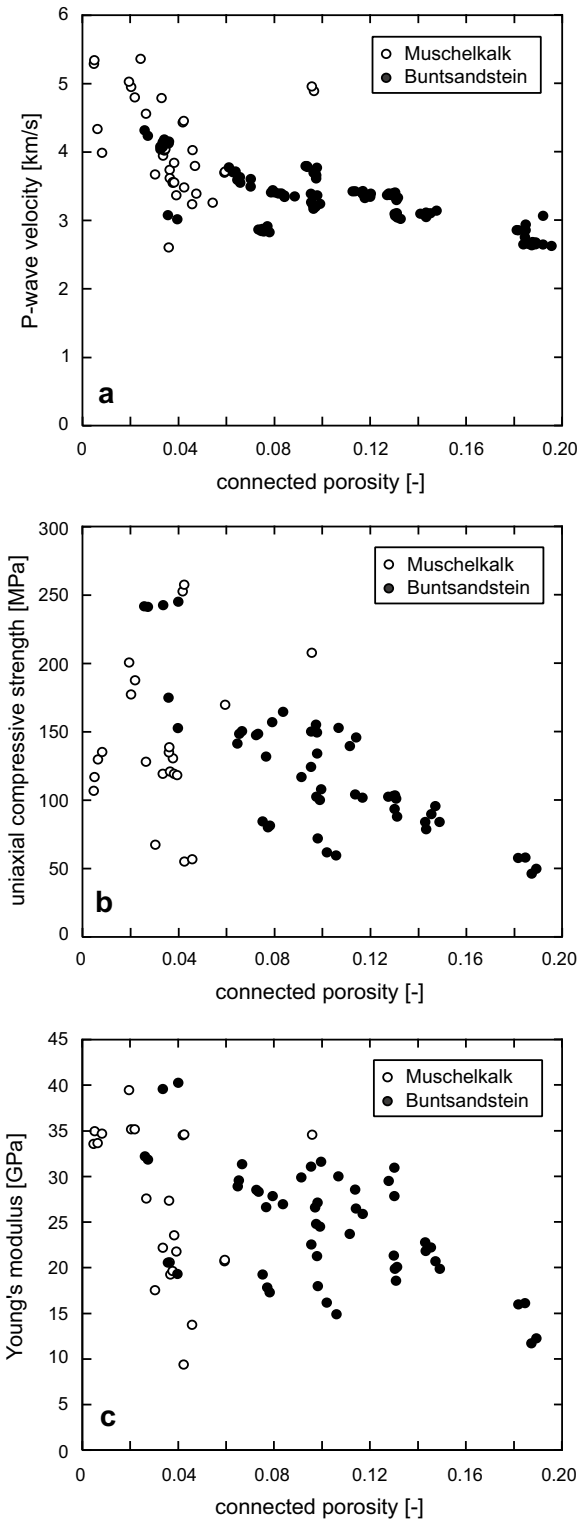


**Fig. 10** **a** Dry P-wave velocity, **b** dry uniaxial compressive strength, and **c** dry Young's modulus as a function of connected porosity for Muschelkalk (white circles) and Buntsandstein (black circles) samples from exploration well EPS-1 (Soultz-sous-Forêts). Data for the Buntsandstein from this study and Heap et al. (2017, 2018, 2019)

units is that the matrix permeability of the Muschelkalk is very low (below the resolution of our permeameter; $\ll 10^{-18}$ m$^2$), due to the low matrix porosity of the Muschelkalk, whereas the matrix permeability of the Buntsandstein varies from $10^{-18}$ to $10^{-13}$ m$^2$ (Haffen et al. 2013; Griffiths et al. 2016; Heap et al. 2017; Kushnir et al. 2018a).

In this contribution, we have measured the thermal properties of the rocks forming the Muschelkalk (Fig. 7). For comparison, we also provide here corresponding thermal property data (thermal conductivity, thermal diffusivity, and specific heat capacity) for samples of the Buntsandstein from exploration borehole EPS-1 (data available in Table 3). We chose to measure the twelve samples of EPS-1 core studied in Heap et al. (2017), which includes: one sandstone from the *Grès à Voltzia* formation (box number 84; depth of 1008), one from the *Couches Intermédiaires* formation (box number 100; depth of 1022 m), three from the *Karlstal* formation (box numbers 157, 198, and 248; depths of 1069, 1107, and 1151 m), two from the *Rehberg* formation (box numbers 299 and 347; depths of 1197 and 1239 m), two from the *Trifels* formation (box numbers 402 and 453; depths of 1290 and 1336 m), two from the *Grès d'Annweiler* formation (box numbers 497 and 508; depths of 1376 and 1386 m), and one from the *Grès anté-Annweiler* formation (box number 540; depth of 1414 m) (see Heap et al. 2017 for further details on these sandstones). Thermal conductivity, thermal diffusivity, and specific heat capacity were measured on oven-dry samples using the Hot Disk TPS 500 Thermal Constants Analyser and the method described above. Figure 11 presents the thermal conductivity, thermal diffusivity, and specific heat capacity as a function of porosity for both the Muschelkalk and Buntsandstein units (data available in Table 3). With the exception of the two samples of anhydrite (boxes 19 and 22; *Marnes Bariolées*, Middle Muschelkalk; Fig. 3d, e), the thermal conductivity of the rocks from these units varies between ~ 2 and ~ 4 W/mK and does not appear to vary systematically with lithology or porosity (Fig. 11a). This range of thermal conductivity values are consistent with the large-scale thermo-hydro-mechanical modelling of the Soultz-sous-Forêts (Vallier et al. 2019) and Rittershoffen (Vallier et al. 2018) geothermal sites, with laboratory data for a wide range of sedimentary rocks from the Upper Rhine Graben (Fuchs and Förster 2010; Haffen et al. 2013; Harlé et al. 2019), and with thermal conductivity maps performed on an 18-cm-long piece of core from the Buntsandstein (from borehole EPS-1) (Haffen et al. 2017). The very low porosity of the anhydrite samples and the high value of thermal conductivity of anhydrite (~ 5 W/mK; Clauser and Huenges 1995) have contributed to the high thermal conductivity of these samples. If we assume a large difference between the thermal conductivity of the rock-forming minerals and the air, we can interrogate the influence of mineralogical variations on the thermal conductivity of the measured samples by plotting thermal conductivity as a function of porosity for the two most common minerals of the Muschelkalk and Buntsandstein (dolomite and quartz, respectively) using the Rayleigh–Maxwell equation:

$$\kappa_e = \kappa_g(1-\phi)/(1+\phi), \tag{2}$$

where $\kappa_e$ and $\kappa_g$ are the thermal conductivities of the equivalent medium and the solid mineral (i.e., dolomite or quartz), respectively, and $\phi$ is the porosity. Values of $\kappa_g$ for dolomite and quartz are taken as 4.78 and 6.15 W/mK, respectively (Clauser and Huenges 1995). These modelled curves are plotted alongside the experimental data on Fig. 11a.

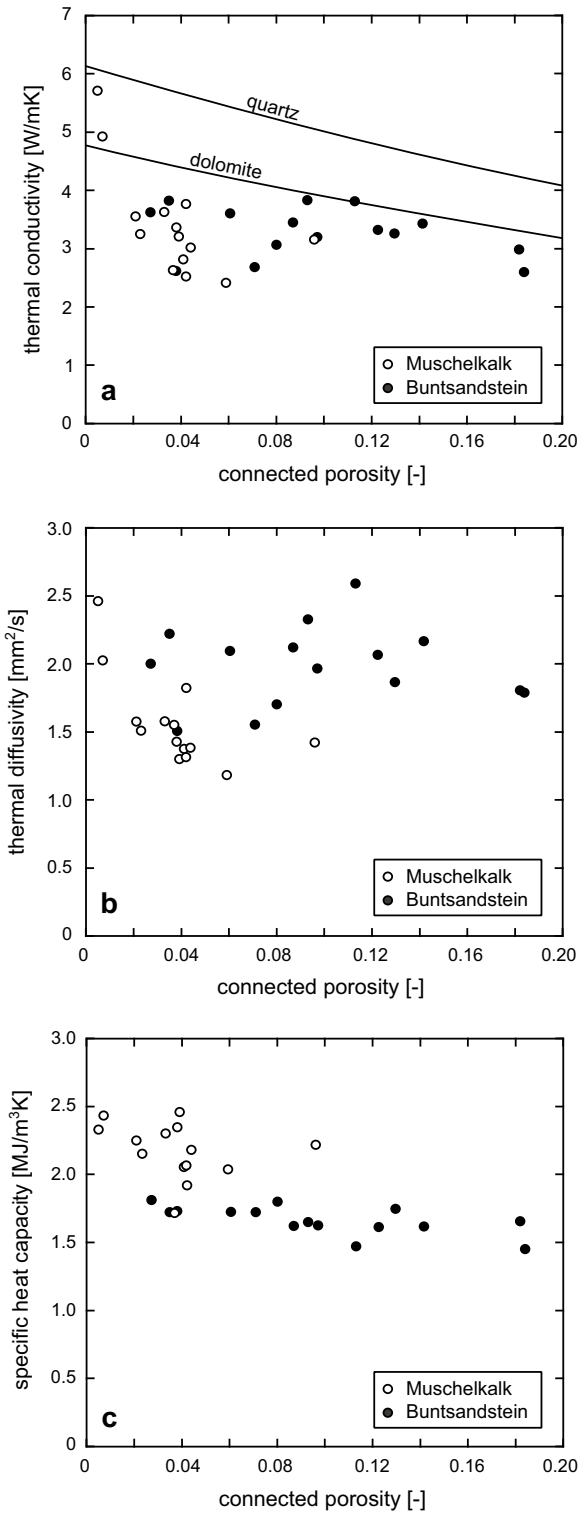


**Fig. 11** **a** Dry thermal conductivity, **b** dry thermal diffusivity, and **c** dry specific heat capacity per unit volume as a function of connected porosity for Muschelkalk (white circles) and Buntsandstein (black circles) samples from exploration well EPS-1 (Soultz-sous-Forêts). Thermal conductivity as a function of porosity is modelled for quartz and dolomite using the Rayleigh–Maxwell equation (Eq. (2); see text for details)

The modelled curves overestimate the thermal conductivity of both the Muschelkalk and Buntsandstein units and are the likely result of minerals such as clays that serve to lower the thermal conductivity. The thermal diffusivities of these rocks vary from ~ 1.25 to ~ 2.5 $mm^2/s$ (Fig. 11b). In general, and despite their higher porosities, the thermal diffusivities of the Buntsandstein samples are higher than those from the Muschelkalk (Fig. 11b). The higher thermal diffusivity of the Buntsandstein can be explained by the high thermal diffusivity of quartz (e.g., Branlund and Hofmeister 2007). The specific heat capacity of samples from the Muschelkalk and Buntsandstein units varies from ~ 1.5 to ~ 2.5 $MJ/m^3K$. The heat capacity of the Muschelkalk samples is typically higher than those for the Buntsandstein, and is likely a function of their lower porosity (Fig. 11c).

#### Implications for geothermal energy exploitation

Our data, using samples sourced from exploration borehole EPS-1 at Soultz-sous-Forêts (Fig. 1a, b), show that the Muschelkalk has a very low matrix porosity ($\ll 0.1$; Table 2) and a very low matrix permeability ($\ll 10^{-18}$ $m^2$). Although these properties suggest that the Muschelkalk unit will provide a barrier to regional fluid flow, and present a poor reservoir/aquifer for geothermal exploitation, we note that the Muschelkalk can contain heavily fractured zones (e.g., Reyer et al. 2012; Meier et al. 2015; Vidal et al. 2015; Aichholzer et al. 2016; Vidal and Genter 2018) that can provide high equivalent (i.e., rock mass) permeabilities (e.g., Kushnir et al. 2018a). The existence of fractured zones within the Muschelkalk at Soultz-sous-Forêts has been confirmed by logging data (e.g., Vidal et al. 2015; Aichholzer et al. 2016). For example, drilling mud and geophysical well logging data from the geothermal wells at Soultz-sous-Forêts (wells GPK-2, GPK-3, and GPK-4; see Fig. 1b for the location of the GPK wells) revealed two permeable zones and one sealed zone in the Muschelkalk at both GPK-2 and GPK-3 and one permeable zone in the Muschelkalk at GPK-4 (Vidal et al. 2015). The thickness of the Muschelkalk in the GPK-1 well is significantly reduced as a result of faulting (Aichholzer et al. 2016). Severe mud losses during the drilling of the wells GRT-1 and GRT-2 as well as positive and negative temperature anomalies also indicate the presence of significant natural fluid circulation in the Muschelkalk at Rittershoffen, located 6.5 km from Soultz-sous-Forêts (Baujard et al. 2017). The highly fractured nature of the Muschelkalk is also apparent further afield, in northwest (e.g., Reyer et al. 2012) and southwest Germany (e.g., Meier et al. 2015). For example, Meier et al. (2015) characterised the fault zones and associated fracture systems for eight exposed fault zones within the Middle Muschelkalk in southwest Germany. These authors concluded that the fractures, which often extended across multiple limestone-marl beds, likely create efficient pathways for fluid flow and that, as a result, fault damage zones in the Muschelkalk may be exploitable geothermal targets (Meier et al. 2015). However, due to the vertical and lateral variability and heterogeneity of the Muschelkalk unit, also exposed herein (Figs. 9, 10), some parts of the Muschelkalk may not represent viable geothermal reservoirs/aquifers and caution must be taken. For example, no mud losses were observed during part of the drilling through the Muschelkalk unit at GRT-2 at Rittershoffen, indicating a very low equivalent permeability (Baujard et al. 2017).

Values of strength and Young's modulus for the Muschelkalk unit (Fig. 8) can be used to guide reservoir stimulation strategies and assessments of borehole stability (e.g.,

Barton et al. 1988; Zheng et al. 1989; Nawrocki and Dusseault 1995; AbuAisha et al. 2016). Here we show that the uniaxial compressive strength (Fig. 8b) and Young's modulus (Fig. 8c) of the Muschelkalk unit is very variable as a result of textural (Fig. 3), microstructural (Figs. 4, 5), and compositional (Table 1) variations. In particular, we highlight that the uniaxial compressive strength of the dolomitic sandstone bank in the Lower Muschelkalk (from box 59; *Wellenmergel and Couches à Térébratules*; Fig. 3j) is very high (~250 MPa; Fig. 8b; Table 2). Therefore, although sandstone banks in the Muschelkalk are rare (Aichholzer et al. 2019; Duringer et al. 2019), if present, they are likely an important consideration when assessing in situ stresses and for assessments of borehole stability and stimulation strategies. The uniaxial compressive strengths and Young's moduli presented herein (Fig. 8; Table 2) are representative of the intact rock (i.e., these values do not take large fractures into account). For analyses and modelling that require rock mass properties, these values (provided in Table 2) can be upscaled using assessments of rock mass structure (e.g., Hoek et al. 2002; Hoek and Diederichs 2006; Reyer et al. 2012; Villeneuve et al. 2018; Heap et al. 2019).

The thermal properties (thermal conductivity, thermal diffusivity, and specific heat capacity) for rocks within a geothermal reservoir can inform, for example, thermo-hydro-mechanical modelling designed to better understand large-scale fluid circulation, heat flow calculations, and temperature estimations (e.g., Fuchs and Förster 2010; Blöcher et al. 2010; Rühaak et al. 2015; Fuchs and Balling 2016; Vallier et al. 2018, 2019; Harlé et al. 2019). Although our thermal properties (Fig. 11; Table 3) were measured on laboratory samples that do not contain fractures that would be encountered in a typical rock mass, we highlight that approaches to upscale thermal conductivity have shown, for example, that laboratory-scale measurements are capable of providing reliable simulated reservoir temperatures (Rühaak et al. 2015).

## Conclusions

Our study has highlighted the high petrophysical variability of the Muschelkalk, an important lithostratigraphic unit for geothermal energy exploitation in the Upper Rhine Graben. Although the matrix porosity, a parameter that typically exerts a first-order control on rock physical properties, is low and falls within a narrow range (from ~0.01 to ~0.1), P-wave velocity, thermal conductivity, thermal diffusivity, specific heat capacity per unit volume, Young's modulus, and uniaxial compressive strength range from 2.60 to 5.37 km/s, 2.42 to 5.72 W/mK, 1.19 to 2.46 $mm^2/s$, 1.63 to 2.46 $MJ/m^3K$, 9.4 to 39.5 GPa, and 55.1 to 257.6 MPa, respectively. The matrix permeability of the Muschelkalk is very low ($\ll 10^{-18}$ $m^2$); however, the equivalent permeability of the Muschelkalk may be high as a result of highly fractured zones. The measured range in petrophysical properties is a result of the textural, microstructural, and compositional variations of the rocks comprising the Muschelkalk. The range of petrophysical properties observed in the Muschelkalk exceeds that of the Buntsandstein, the unit situated below the Muschelkalk and above the fractured reservoir granite, despite the large range in matrix porosity observed within the Buntsandstein. Although these data can be used to assist reservoir prospection, stimulation, and optimisation strategies at geothermal sites within the Upper Rhine Graben, we conclude that caution is perhaps required when targeting the Muschelkalk as a reservoir/aquifer due to its high variability in terms of not only

petrophysical properties, but also rock mass structure. For example, the equivalent permeability of the Muschelkalk unit will be too low to support flow in the absence of highly fractured zones. It is our hope that the petrophysical properties provided herein are useful for (1) thermo-hydro-mechanical modelling designed to better understand large-scale fluid circulation, heat flow calculations, and temperature estimations and (2) reservoir stimulation strategies and assessments of borehole stability at geothermal sites throughout the Upper Rhine Graben.

**Abbreviations**

SEM: scanning electron microscope; XRPD: X-ray powder diffraction; LVDT: linear variable differential transducer; $\sigma_u$: uniaxial compressive strength; $\phi$: porosity; $K_{IC}$: fracture toughness; $r$: pore radius; $\kappa_e$: thermal conductivity of the equivalent medium; $\kappa_g$: thermal conductivity of the solid material.

**Acknowledgements**

We wish to thank Lucille Carbillet, Corentin Noël, Julien Schneider, Bertrand Renaudié, Thierry Reuschlé, Philippe Duringer, Coralie Aichholzer, and Gilles Morvan.

**Authors' contributions**

MJH led the project and wrote the manuscript. MJH, PB, and ARLK chose and collected the samples from the Merkwiller-Pechelbronn core repository. ARLK measured porosity, P-wave velocity, and thermal properties. MV measured uniaxial compressive strength. MJH calculated Young's modulus. MJH and ARLK performed the microstructural analysis. HAG performed the XRPD analyses. PH provided the geological interpretation of the core. All authors had a hand in the preparation of the manuscript and the interpretation of the data. All authors read and approved the final manuscript.

**Funding**

This study was funded by LABEX Grant ANR-11-LABX-0050_G-EAU-THERMIE-PROFONDE (this research therefore benefited from state funding managed by the Agence National de la Recherche (ANR) as part of the "Investissements d'avenir" program) and ANR Grant CANTARE (ANR-15-CE06-0014-01).

**Availability of data and materials**

The data collected for this study are available in Tables 1 and 2. Materials (samples, thin sections, etc.) could also be made available upon request to the first author.

**Ethics approval and consent to participate**

Not applicable.

**Competing interests**

The authors declare that they have no competing interests.

**Author details**

[1] Géophysique Expérimentale, Institut de Physique de Globe de Strasbourg (UMR 7516 CNRS, Université de Strasbourg/EOST), 5 Rue René Descartes, 67084 Strasbourg Cedex, France. [2] Lehrstuhl für Ingenieurgeologie, Technische Universität München, Arcisstr. 21, 80333 Munich, Germany. [3] École Polytechnique Fédérale de Lausanne (EPFL), Faculté de l'Environnement Naturel, Architectural et Construit (ENAC), Laboratory of Experimental Rock Mechanics (LEMR), Station 18, 1015 Lausanne, Switzerland. [4] Institut de Physique de Globe de Strasbourg (UMR 7516 CNRS, Université de Strasbourg/EOST), 1 Rue Blessig, 67084 Strasbourg Cedex, France.

Received: 20 May 2019 Accepted: 6 September 2019
Published online: 17 September 2019

**References**

AbuAisha M, Loret B, Eaton D. Enhanced Geothermal Systems (EGS): Hydraulic fracturing in a thermo-poroelastic framework. J Petrol Sci Eng. 2016;146:1179–91.

Aichholzer C, Duringer P, Genter A. Detailed descriptions of the lower-middle Triassic and Permian formations using cores and gamma rays from the EPS-1 borehole, Soultz-sous-Forêts (Upper Rhine Graben, France). Geoth Energy 2019 **(in revision)**.

Aichholzer C, Duringer P, Orciani S, Genter A. New stratigraphic interpretation of the Soultz-sous-Forêts 30-year-old geothermal wells calibrated on the recent one from Rittershoffen (Upper Rhine Graben, France). Geotherm Energy. 2016;4:13.

Austin NJ, Kennedy LA. Textural controls on the brittle deformation of dolomite: variations in peak strength. Geol Soc Lond Spec Pub. 2005;243(1):37–49.

Bagdassarov N, Dingwell DB. Thermal properties of vesicular rhyolite. J Volcanol Geotherm Res. 1994;60(2):179–91.

Baillieux P, Schill E, Edel JB, Mauri G. Localization of temperature anomalies in the Upper Rhine Graben: insights from geophysics and neotectonic activity. Int Geol Rev. 2013;55:1744–62.

Barton CA, Zoback MD, Burns KL. In-situ stress orientation and magnitude at the Fenton Geothermal Site, New Mexico, determined from wellbore breakouts. Geophys Res Lett. 1988;15(5):467–70.

Baud P, Tf Wong, Zhu W. Effects of porosity and crack density on the compressive strength of rocks. Int J Rock Mech Min Sci. 2014;67:202–11.
Baud P, Rolland A, Heap MJ, Xu T, Nicolé M, Ferrand T, Reuschlé T, Toussaint R, Conil N. Impact of stylolites on the mechanical strength of limestone. Tectono. 2016;690:4–20.
Baujard C, Genter A, Dalmais E, Maurer V, Hehn R, Rosillette R, Vidal J, Schmittbuhl J. Hydrothermal characterization of wells GRT-1 and GRT-2 in Rittershoffen, France: implications on the understanding of natural flow systems in the Rhine graben. Geothermics. 2017;65:255–68.
Bell FG. A survey of the engineering properties of some anhydrite and gypsum from the north and midlands of England. Eng Geol. 1994;38(1–2):1–23.
Berger J-P, Reichenbacher B, Becker D, Grimm M, Grimm K, Picot L, Storni A, Prikenseer C, Schaefer A. Eocene-Pliocene time scale and stratigraphy of the Upper Rhine Graben (URG) and the Swiss Molasse Basin (SMB). Int J Earth Sci. 2005;94(4):711–31.
Bergmann J, Friedel P, Kleeberg R. BGMN—a new fundamental parameters based Rietveld program for laboratory X-ray sources, its use in quantitative analysis and structure investigations. CPD Newsletter. 1998;20:5.
Blöcher MG, Zimmermann G, Moeck I, Brandt W, Hassanzadegan A, Magri F. 3D numerical modeling of hydrothermal processes during the lifetime of a deep geothermal reservoir. Geofluids. 2010;10(3):406–21.
Branlund JM, Hofmeister AM. Thermal diffusivity of quartz to 1,000 C: effects of impurities and the α-β phase transition. Phys Chem Min. 2007;34(8):581–95.
Brigaud F, Vasseur G. Mineralogy, porosity and fluid control on thermal conductivity of sedimentary rocks. Geophys J Int. 1989;98(3):525–42.
Brun JP, Wenzel F. Crustal-scale structure of the southern Rhine Graben from ECORS-DEKORP seismic reflection data. Geology. 1991;19(7):758–62.
Buchmann TJ, Connolly PT. Contemporary kinematics of the Upper Rhine Graben: a 3D finite element approach. Global Planet Change. 2007;58:287–309.
Cardozo GGL, Behrmann JH. Kinematic analysis of the Upper Rhine Graben boundary fault system. J Struct Geol. 2006;28(6):1028–39.
Chandler MR, Meredith PG, Brantut N, Crawford BR. Fracture toughness anisotropy in shale. J Geophys Res. 2016;121(3):1706–29.
Chang C, Zoback MD, Khaksar A. Empirical relations between rock strength and physical properties in sedimentary rocks. J Petrol Sci Eng. 2006;51(3–4):223–37.
Clauser C, Huenges E. Thermal conductivity of rocks and minerals. Rock Phys Phase Relat. 1995;3:105–26.
De Paola N, Faulkner DR, Collettini C. Brittle versus ductile deformation as the main control on the transport properties of low-porosity anhydrite rocks. J Geophys Res. 2009;114:B6. https://doi.org/10.1029/2008jb005967.
Delle Piane C, Burlini L, Kunze K. The influence of dolomite on the plastic flow of calcite: rheological, microstructural and chemical evolution during large strain torsion experiments. Tectono. 2009;467(1–4):145–66.
Dezayes C, Genter A, Valley B. Structure of the low permeable naturally fractured geothermal reservoir at Soultz. CR Geosci. 2010;342:517–30.
Döbelin N, Kleeberg R. Profex: a graphical user interface for the Rietveld refinement program BGMN. J App Crystal. 2015;48(5):1573–80.
Duringer P, Aichholzer C, Orciani S, Genter A. The complete stratigraphic log of geothermal wells at Rittershoffen (Upper Rhine Graben, eastern France): a new insight for the regional stratigraphy and a key for future geothermal wells. Bulletin de la Société Géologique de France 2019 **(accepted)**.
Eberhardt E, Stead D, Stimpson B. Quantifying progressive pre-peak brittle fracture damage in rock during uniaxial compression. Int J Rock Mech Min Sci. 1999;36(3):361–80.
Eberhart-Phillips D, Han DH, Zoback MD. Empirical relationships among seismic velocity, effective pressure, porosity, and clay content in sandstone. Geophysics. 1989;54(1):82–9.
Esteban L, Pimienta L, Sarout J, Delle Piane C, Haffen S, Géraud Y, Timms NE. Study cases of thermal conductivity prediction from P-wave velocity and porosity. Geothermics. 2015;53:255–69.
Farquharson JI, Heap MJ, Lavallée Y, Varley NR, Baud P. Evidence for the development of permeability anisotropy in lava domes and volcanic conduits. J Volcanol Geotherm Res. 2016;323:163–85.
Fuchs S, Balling N. Improving the temperature predictions of subsurface thermal models by using high-quality input data. Part 1: uncertainty analysis of the thermal-conductivity parameterization. Geothermics. 2016;64:42–54.
Fuchs S, Förster A. Rock thermal conductivity of Mesozoic geothermal aquifers in the Northeast German Basin. Chemie Der Erde-Geochemistry. 2010;70:13–22.
Genter A, Traineau H. Analysis of macroscopic fractures in granite in the HDR geothermal well EPS-1, Soultz-sous-Forêts, France. J Volcanol Geotherm Res. 1996;72:121–41.
Genter A, Castaing C, Dezayes C, Tenzer H, Traineau H, Villemin T. Comparative analysis of direct (core) and indirect (borehole imaging tools)collection of fracture data in the Hot Dry Rock Soultz reservoir (France). J Geophys Res: Solid Earth. 1997;102(B7):15419–31.
Genter A, Evans K, Cuenot N, Fritsch D, Sanjuan B. Contribution of the exploration of deep crystalline fractured reservoir of Soultz to the knowledge of enhanced geothermal systems (EGS). CR Geosci. 2010;342:502–16.
Glaas C, Genter A, Girard JF, Patrier P, Vidal J. How do the geological and geophysical signatures of permeable fractures in granitic basement evolve after long periods of natural circulation? Insights from the Rittershoffen geothermal wells (France). Geotherm Energy. 2018;6:14.
Griffiths L, Heap MJ, Wang F, Daval D, Gilg HA, Baud P, Schmittbuhl J, Genter A. Geothermal implications for fracture-filling hydrothermal precipitation. Geothermics. 2016;64:235–45.
Griffiths L, Heap MJ, Xu T, Cf Chen, Baud P. The influence of pore geometry and orientation on the strength and stiffness of porous rock. J Struct Geol. 2017;96:149–60.
Guillou-Frottier L, Carré C, Bourgine B, Bouchot V, Genter A. Structure of hydrothermal convection in the Upper Rhine Graben as inferred from corrected temperature data and basin-scale numerical models. J Volcanol Geotherm Res. 2013;256:29–49.

Gustavsson M, Karawacki E, Gustafsson SE. Thermal conductivity, thermal diffusivity, and specific heat of thin samples from transient measurements with hot disk sensors. Rev Sci Instrum. 1994;65(12):3856–9.
Haffen S, Géraud Y, Diraison M, Dezayes C. Determination of fluid-flow zones in a geothermal sandstone reservoir using thermal conductivity and temperature logs. Geothermics. 2013;46:32–41.
Haffen S, Géraud Y, Rosener M, Diraison M. Thermal conductivity and porosity maps for different materials: a combined case study of granite and sandstone. Geothermics. 2017;66:143–50.
Han DH, Nur A, Morgan D. Effects of porosity and clay content on wave velocities in sandstones. Geophysics. 1986;51(11):2093–107.
Harlé P, Kushnir ARL, Aichholzer C, Heap MJ, Hehn R, Maurer V, Baud P, Richard A, Genter A, Duringer D. Heat flow estimations in the Upper Rhine Graben using laboratory measurements of thermal conductivity on sedimentary rocks. Geoth Energy 2019 **(in revision)**.
Heap MJ, Kennedy BM. Exploring the scale-dependent permeability of fractured andesite. Earth Planet Sci Lett. 2016;447:139–50.
Heap MJ, Xu T, Cf Chen. The influence of porosity and vesicle size on the brittle strength of volcanic rocks and magma. Bull Volcanol. 2014;76(9):856.
Heap MJ, Kushnir ARL, Gilg HA, Wadsworth FB, Reuschlé T, Baud P. Microstructural and petrophysical properties of the Permo-Triassic sandstones (Buntsandstein) from the Soultz-sous-Forêts geothermal site (France). Geotherm Energy. 2017;5(1):26.
Heap MJ, Reuschlé T, Kushnir ARL, Baud P. The influence of hydrothermal brine on the short-term strength and elastic modulus of sandstones from exploration well EPS-1 at Soultz-sous-Forêts (France). Geotherm Energy. 2018;6(1):29.
Heap MJ, Villeneuve M, Kushnir ARL, Farquharson JI, Baud P, Reuschlé T. Rock mass strength and elastic modulus of the Buntsandstein: an important lithostratigraphic unit for geothermal exploitation in the Upper Rhine Graben. Geothermics. 2019;77:236–56.
Hinsken S, Ustaszewski K, Wetzel A. Graben width controlling syn-rift sedimentation: the Palaeogene southern Upper Rhine Graben as an example. Int J Earth Sci. 2007;96(6):979–1002.
Hinsken S, Schmalholz SM, Ziegler PA, Wetzel A. Thermo-Tectono-Stratigraphic Forward Modelling of the Upper Rhine Graben in reference to geometric balancing: brittle crustal extension on a highly viscous mantle. Tectono. 2011;509(1–2):1–13.
Hoek E, Diederichs MS. Empirical estimation of rock mass modulus. Int J Rock Mech Min Sci. 2006;43(2):203–15.
Hoek E, Carranza-Torres C, Corkum B. Hoek-Brown failure criterion-2002 edition. Proce NARMS-Tac. 2002;1(1):267–73.
Hooijkaas GR, Genter A, Dezayes C. Deep-seated geology of the granite intrusions at the Soultz EGS site based on data from 5 km-deep boreholes. Geothermics. 2006;35:484–506.
Kushnir ARL, Kennedy LA, Misra S, Benson PM, White JC. The mechanical and microstructural behaviour of calcite-dolomite composites: an experimental investigation. J Struct Geol. 2015;70:200–16.
Kushnir ARL, Heap MJ, Baud P. Assessing the role of fractures on the permeability of the Permo-Triassic sandstones at the Soultz-sous-Forêts (France) geothermal site. Geothermics. 2018a;74:181–9.
Kushnir ARL, Heap MJ, Baud P, Gilg HA, Reuschlé T, Lerouge C, Dezayes C, Duringer P. Characterizing the physical properties of rocks from the Paleozoic to Permo-Triassic transition in the Upper Rhine Graben. Geotherm Energy. 2018b;6:16.
Ledésert B, Dubois J, Genter A, Meunier A. Fractal analysis of fractures applied to Soultz-sous-Forêts hot dry rock geothermal program. J Volcanol Geotherm Res. 1993;57(1–2):1–17.
Ledésert B, Joffre J, Amblès A, Sardini P, Genter A, Meunier A. Organic matter in the Soultz HDR granitic thermal exchanger (France): natural tracer of fluid circulations between the basement and its sedimentary cover. J Volcanol Geotherm Res. 1996;70(3–4):235–53.
Link K, Rybach L, Imhasly S, Wyss R. Geothermal Energy in Switzerland-Country Update. Proc World Geotherm Congress. 2015;2015:19–24.
Magnenet V, Fond C, Genter A, Schmittbuhl J. Two-dimensional THM modelling of the large scale natural hydrothermal circulation at Soultz-sous-Forêts. Geotherm Energy. 2014;2(1):17.
Meier S, Bauer JF, Philipp SL. Fault zone characteristics, fracture systems and permeability implications of Middle Triassic Muschelkalk in Southwest Germany. J Struct Geol. 2015;70:170–89.
Meixner J, Schill E, Grimmer JC, Gaucher E, Kohl T, Klingler P. Structural control of geothermal reservoirs in extensional tectonic settings: an example from the Upper Rhine Graben. J Struct Geol. 2016;82:1–15.
Ménillet F. Carte géologique de la France à 1/50 000 198 Haguenau. 2nd ed. Orléans: Bureau de recherches géologiques et minières; 2015.
Nawrocki PA, Dusseault MB. Modelling of damaged zones around openings using radius-dependent Young's modulus. Rock Mech Rock Eng. 1995;28(4):227–39.
Peters G, van Balen RT. Tectonic geomorphology of the northern Upper Rhine Graben, Germany. Glob Planet Change. 2007;58(1–4):310–34.
Pimienta L, Sarout J, Esteban L, Delle Piane C. Prediction of rocks thermal conductivity from elastic wave velocities, mineralogy and microstructure. Geophys J Int. 2014;197(2):860–74.
Popov Y, Tertychnyi V, Romushkevich R, Korobkov D, Pohl J. Interrelations between thermal conductivity and other physical properties of rocks: experimental data. Thermo-hydro-mechanical coupling in fractured rock. Basel: Birkhäuser; 2003. p. 1137–61.
Pribnow D, Schellschmidt R. Thermal tracking of upper crustal fluid flow in the Rhine Graben. Geophys Res Lett. 2000;27(13):1957–60.
Regnet JB, Robion P, David C, Fortin J, Brigaud B, Yven B. Acoustic and reservoir properties of microporous carbonate rocks: implication of micrite particle size and morphology. J Geophys Res. 2015;120(2):790–811.
Regnet JB, David C, Robion P, Menéndez B. Microstructures and physical properties in carbonate rocks: a comprehensive review. Marine Petrol Geol. 2019;103:366–76.

Reyer D, Bauer JF, Philipp SL. Fracture systems in normal fault zones crosscutting sedimentary rocks, Northwest German Basin. J Struct Geol. 2012;45:38–51.
Rühaak W, Guadagnini A, Geiger S, Bär K, Gu Y, Aretz A, Homuth S, Sass I. Upscaling thermal conductivities of sedimentary formations for geothermal exploration. Geothermics. 2015;58:49–61.
Sammis CG, Ashby MF. The failure of brittle porous solids under compressive stress states. Acta Metall. 1986;34(3):511–26.
Sausse J, Fourar M, Genter A. Permeability and alteration within the Soultz granite inferred from geophysical and flow log analysis. Geothermics. 2006;35(5–6):544–60.
Schumacher ME. Upper Rhine Graben: role of preexisting structures during rift evolution. Tectonics. 2002;21(1):6.
Sittler C. The sedimentary trough of the Rhine Graben. Tectono. 1969;8(4–6):543–60.
Trippetta F, Collettini C, Meredith PG, Vinciguerra S. Evolution of the elastic moduli of seismogenic Triassic Evaporites subjected to cyclic stressing. Tectono. 2013;592:67–79.
Vallier B, Magnenet V, Schmittbuhl J, Fond C. THM modeling of hydrothermal circulation at Rittershoffen geothermal site. France. Geotherm Energy. 2018;6(1):22.
Vallier B, Magnenet V, Schmittbuhl J, Fond C. Large scale hydro-thermal circulation in the deep geothermal reservoir of Soultz-sous-Forêts (France). Geothermics. 2019;78:154–69.
Vidal J, Genter A. Overview of naturally permeable fractured reservoirs in the central and southern Upper Rhine Graben: insights from geothermal wells. Geothermics. 2018;74:57–73.
Vidal J, Genter A, Schmittbuhl J. How do permeable fractures in the Triassic sediments of Northern Alsace characterize the top of hydrothermal convective cells? Evidence from Soultz geothermal boreholes (France). Geotherm Energy. 2015;3:8.
Villeneuve M, Heap MJ, Kushnir ARL, Qin T, Baud P, Zhou G, Xu T. Estimating in situ rock mass strength and elastic modulus of granite from the Soultz-sous-Forêts geothermal reservoir (France). Geotherm Energy. 2018;6:11.
Zheng Z, Kemeny J, Cook NG. Analysis of borehole breakouts. J Geophys Res: Solid Earth. 1989;94(B6):7171–82.
Zhu W, Baud P, Tf Wong. Micromechanics of cataclastic pore collapse in limestone. J Geophys Res. 2010;115:B4. https://doi.org/10.1029/2009JB006610.

## Publisher's Note